

The long-term broad-line responsivity in MKN 110

D. Homan,^{1,2★} A. Lawrence^{1,2}, M. Ward,³ A. Bruce,² H. Landt,³ C. MacLeod,⁴ M. Elvis,⁵ B. Wilkes,^{5,6}
J. P. Huchra^{5†} and B. M. Peterson[‡]

¹Leibniz-Institut für Astrophysik Potsdam, An der Sternwarte 16, D-14482 Potsdam, Germany

²Institute for Astronomy, SUPA (Scottish Universities Physics Alliance), University of Edinburgh, Royal Observatory, Blackford Hill, Edinburgh EH9 3HJ, UK

³Department of Physics, Durham University, South Road, Durham DH1 3LE, UK

⁴BlackSky, 1505 Westlake Ave N #600, Seattle, WA 98109, USA

⁵Center for Astrophysics, Harvard and Smithsonian, 60 Garden St, Cambridge, MA 02138, USA

⁶HH Wills Physics Laboratory, University of Bristol, Tyndall Avenue, Bristol BS8 1TL, UK

Accepted 2022 November 27. Received 2022 November 3; in original form 2022 September 19

ABSTRACT

We examine the long-term history of the optical spectrum of the extremely variable Active Galactic Nucleus (AGN) MKN 110. By combining various archival data with new data, we cover an unprecedented long period of ~ 30 yr (1987–2019). We find that the He II $\lambda 4686$ emission line changes by a factor of forty and varies more strongly than the optical continuum. Following Ferland et al., we take He II $\lambda 4686$ as a proxy for the FUV continuum and compare the flux of several other line species against it. This comparison reveals a clear pattern, whereby lines respond close to linearly at low FUV fluxes, and saturate at high FUV fluxes. The saturation level of the response appears to depend on the excitation energy of the line species. In addition to this global pattern, we note changes among observational epochs, indicating a structural evolution in the broad line region (BLR). The line profiles in our spectra show an offset between the narrow and broad components of the He II $\lambda 4686$ and H β lines. This offset shows a significant negative correlation with the FUV flux and a positive correlation with the line velocity width. Our analysis reveals a complex BLR response to a changing continuum. The clear presence of a non-responsive component of the broad lines indicates the existence of multiple contributions to the line emission. We find there are several kinematic models of the BLR and inner regions of the AGN that match our data.

Key words: galaxies: nuclei – quasars: emission lines – galaxies: Seyfert.

1 INTRODUCTION

Two striking features of the optical/UV spectra of Active Galactic Nuclei (AGNs) are the blue continuum and the broad emission lines (BELs). These features are closely connected: they are always seen together, and it is assumed that an extrapolation of the blue continuum into the far-UV provides the photons that ionize the gas producing the emission lines (see e.g. Osterbrock & Ferland 2006; Peterson 2006; Netzer 2013, and extensive references therein). Strong evidence for this connection is found in the fact that variations in the strengths of the BELs track the variations in the blue continuum, but with a delay (lag) of the order days-months, depending on the luminosity of the object (Gaskell & Sparke 1986; Clavel et al. 1991; Peterson et al. 1998; Netzer 2020). The lags, interpreted as light traveltime delays, tell us the size of the Broad Line Region (BLR), using a technique referred to as Reverberation Mapping (RM; Blandford & McKee 1982; Peterson 1993).

Simple single-cloud ionization models typically require an ionization parameter of $U \sim 0.1$,¹ along with a typical BLR particle

number density of $n \sim 10^{10} \text{ cm}^{-3}$, and a typical cloud thickness $N_H \sim 10^{23} \text{ cm}^{-2}$ (Peterson 2006; Netzer 2013). The size of the lag observed in reverberation experiments correlates well with the luminosity of the AGN (Kaspi et al. 2000; Bentz et al. 2013; Pancoast et al. 2014; Lira et al. 2018; Dalla Bontà et al. 2020; Netzer 2022), which suggests that the value of $U \sim 0.1$ is quasi-universal. How the universal U -value comes about is a long-standing puzzle (Rees, Netzer & Ferland 1989; Baskin, Laor & Stern 2013; Baskin & Laor 2018), and indeed, although the basic parameters of the BLR – size, density, covering factor – are reasonably well known, its detailed structure, its velocity field, as well as its physical origin, remain controversial (Netzer 2020, 2022).

A potentially important clue to the structure of the BLR is the *responsivity* of lines to changes in the continuum (Goad, O’Brien & Gondhalekar 1993). It was already clear in the pioneering study of NGC 5548 (Clavel et al. 1991; Krolik et al. 1991) that some lines are more responsive than others. While the UV continuum 1350 Å in this object at underwent peak-to-trough changes of a factor of ~ 2.5 , line responses ranged from Ly α , changing with a factor of ~ 1.8 , to Mg II $\lambda 2798$ with a factor of ~ 1.2 . The difference in responsivity may have a natural explanation in terms of the ‘Local Optimally emitting Cloud (LOC)’ picture (Baldwin et al. 1995; Korista & Goad 2000, 2004; Goad & Korista 2015), as the changing ionizing continuum picks out clouds from a broad distribution of density and distance.

* E-mail: dshoman@gmail.com

† Deceased, 2010

‡ Retired

¹ U is defined as the ratio of ionizing photons to the amount of material that can be ionized: $U = N_{\text{ion}}/(4\pi R^2 c N_{\text{atom}})$.

However, the response behaviour of lines is complicated. For example, Mg II is generally assumed to be weakly responsive, and sometimes seems to show no response at all (Cackett et al. 2015; Sun et al. 2015), but extreme variability over several years seen in ‘Changing Look Quasars’ can show large changes in Mg II $\lambda 2798$ (MacLeod et al. 2016; Guo et al. 2019; Homan et al. 2020). Meanwhile, the He II $\lambda 4686$ line can show extremely strong changes, possibly even larger than the optical continuum (Peterson & Ferland 1986; Peterson 1988; Grier et al. 2012; Peterson et al. 2014; Barth et al. 2015; Ferland et al. 2020).

In order to study the BLR response more fully and to clarify these confusing patterns, what is needed are sets of observations that are both high-cadence and long-term, and that involve a large amplitude of variability. Recently, Ferland et al. (2020) have discussed the suitability of using He II as a proxy for the unobservable FUV continuum since this emission line is effectively a photon counter. Here we explore further the use of He II as an indicator of the FUV continuum and apply it to the long-term evolution of the broad emission lines in the local Seyfert galaxy MKN 110, which has been observed over many years, and has undergone large flux changes.

The paper is organized as follows. In Section 2, we summarize previous work on MKN 110. In Section 3, we present new spectroscopic observations, and tabulate key values along with data from the literature. We then present our methods for flux calculation and line profile measurements in Section 4. Section 5 provides an overview of the long-term evolution of MKN 110 and in Section 6, we present an analysis of how various lines respond to the continuum, using He II $\lambda 4686$ as a proxy. In Section 7, we examine how velocity offsets, velocity width, and luminosity state correlate over time. We summarize our results in Section 8. In Sections 9–12 we discuss our new results in the context of rival interpretations of BLR structure and origin, and point towards future work.

2 MKN 110: KEY RESULTS FROM PREVIOUS WORK

MKN 110 has a long history of observations, focusing on optical, UV, and X-rays (e.g. Bischoff & Kollatschny 1999; Ferrarese et al. 2001; Boller, Balestra & Kollatschny 2007; Porquet et al. 2021; Vincentelli et al. 2021). The type E galaxy hosts a type 1 Seyfert nucleus at $z = 0.0353$, with an average bolometric nuclear luminosity of $\sim 2 \times 10^{44} \text{ ergs}^{-1}$ (Véron-Cetty et al. 2007). Optical imaging of the galaxy shows a clear tidal tail suggesting a past merger or tidal interaction, but there is only one obvious nucleus. The nucleus is clearly detected in X-rays by *ROSAT*, *XMM-Newton*, and *Swift*-BAT with a spectral slope typical of type 1 AGN: for a single power-law fit $\Gamma \sim 2.4$ (Lawrence et al. 1997; Grupe, Thomas & Beuermann 2001; Boller et al. 2007; Winter et al. 2012; Porquet et al. 2021). The nucleus is radio-quiet, observed in NVSS at 10.1 mJy at 1.4 GHz (Condon 1992) and observed with the VLBA to be between 0.7 and 1.6 mJy at 5 GHz (Panessa et al. 2022).

Of particular relevance to this work are several programmes of optical spectroscopic observations (Bischoff & Kollatschny 1999; Kollatschny et al. 2001; Kollatschny & Bischoff 2002; Kollatschny 2003a,b), that cover the evolution of the continuum and the BLR. Bischoff & Kollatschny (1999, BK99) collected 24 spectra over 8 yr (1987 to 1995), measured lags for several lines, and showed that the lags correlate with line width. This is one of the clearest known examples of BLR stratification. Kollatschny et al. (2001, K01) undertook a more intense short-term reverberation campaign, with 26 epochs spread over a few months. Kollatschny & Bischoff (2002, KB02) and Kollatschny (2003a, K03a) used the same data set,

but split several lines into 200 km s^{-1} segments, to produce velocity-resolved delay maps. These maps showed that the line wings have a shorter delay than the cores. The authors argued that the results were consistent with the kinematics of a Keplerian disc. There is marginal evidence that the blue wings lag the red wings by $\sim 2 \text{ d}$, matching a disc wind model, with a combination of rotation and outflow (K03a).

Kollatschny (2003b, K03b), again using the K01 data-set, noted that several broad emission lines show a velocity offset towards the red compared to the narrow lines, and that the offset correlates with the line lag, and therefore also with line width – the offset is especially striking in He II $\lambda 4686$. K03b interprets the offset as *gravitational redshift*. On this basis they derive a central mass of $\log[M_{\text{BH}}/M_{\odot}] = 8.15^{+0.03}_{-0.10}$. Comparing this with the much smaller K01 reverberation mass, $\log[M_{\text{BH}}/M_{\odot}] = 7.26^{+0.09}_{-0.11}$, K03b derives an inclination for the BLR disc structure of $i = 21 \pm 5^{\circ}$, i.e. close to pole on.

There is a large discrepancy between the K01 and K03b mass estimates, which has a significant impact on the derived physical parameters of the BLR and the classification of MKN 110. Discrepant results for different methods of mass estimation are found in other works as well. As MKN 110 is a well-studied object, there is a large number of independent mass estimates. Based on X-ray data, $\log[M_{\text{BH}}/M_{\odot}] = 7.37$ was reported using the excess variance in the flux (Ponti et al. 2012), and $\log[M_{\text{BH}}/M_{\odot}]$ in the range 7.4–8.3 using a method based on a Comptonization model to scale from stellar-mass BHs to SMBHs (Gliozzi et al. 2011; Williams, Gliozzi & Rudzinsky 2018). Reverberation mapping studies, including BK99 and K01, reported $\log[M_{\text{BH}}/M_{\odot}]$ in the range 6.89–7.78 (BK99, K01; Kaspi et al. 2000; Peterson et al. 2004). The broad range in the RM values is in large part due to the uncertainty in the virial factor f ,² which accounts for the unknown orientation and geometry of the BLR. The assumed values of f vary from $\sqrt{3}/2$ to 5.5 (covering spherical and flattened BLR geometries), among the different studies. Based on the stellar velocity dispersion in the bulge, measured by Ferrarese et al. (2001), a $\log[M_{\text{BH}}/M_{\odot}]$ of ~ 6.5 can be deduced (Ferrarese & Merritt 2000; Greene & Ho 2006; Véron-Cetty et al. 2007). Finally, using spectropolarimetry of the H α line, a method that should be independent from the BLR’s inclination, Afanasiev, Popović & Shapovalova (2019) reported a (log) mass of $8.32 \pm 0.21 M_{\odot}$.

The BELs of MKN 110 are relatively narrow, which means the nucleus could tentatively be identified as a narrow-line Sy1 (e.g. Grupe 2004, BK99). However, the X-ray power-law index and low X-ray absorbing column density (Lawrence et al. 1997; Porquet et al. 2021), as well as the strong [O III] lines and weak Fe II emission (Véron-Cetty et al. 2007) indicate that this classification is likely incorrect. NLSy1s typically have low black-hole masses and accretion rates near or over the Eddington limit (Nicastro 2000), whereas the range of black-hole mass estimates for MKN 110 better matches BLSy1s. Meyer-Hofmeister & Meyer (2011) find an average Eddington ratio for MKN 110 of ~ 40 per cent (using the mass from Peterson et al. 2004). The most likely explanation appears to be that MKN 110 is a BLSy1 viewed close to pole-on.

MKN 110 has long been known as a highly variable source. Optical photometric variability on time-scales smaller than days was noted by Webb & Malkan (2000) and MKN 110 was recently the topic of an extensive continuum-RM campaign (Vincentelli et al. 2021, 2022). The continuum RM studies not only showed clear

²virial factor $f \equiv 1/(4 \sin^2 i)$, following McLure & Dunlop (2004), who assume a flattened BLR geometry. However, other studies have assumed different BLR geometries resulting in different interpretations of f .

Table 1. Overview of our available data on MKN 110.

Data ^a	Epoch	N_{spec}	Spectra ^b	Fluxes ^c	Resolution	Slit/Fibre	Observing conditions
WHP98	1992–1996	95	✗	✓	1600 (at 4800 Å)	–	–
BK99	1987–1995	24	✗	✓	1300 (at 4000 Å)	2–2.5 arcsec	Non-photometric
K01	1999–2000	26	✗	✓	650 (at 4000 Å)	2 arcsec	–
SDSS	2001	1	✓	✓	1500 (at 3800 Å)	2 arcsec	Photometric
FAST	2002–2019	59	✓	✓	1600 (at 4800 Å)	3 arcsec	Mixed
WHT	2016–2017	2	✓	✓	1500 (at 5200 Å)	1–1.5 arcsec	Photometric (2016)/cloudy (2017)

Notes. ^aName of data set. WHP98 is a previously unpublished data set of RM observations, BK99 and K01 refer to Bischoff & Kollatschny (1999) and Kollatschny et al. (2001), respectively. FAST and WHT refer to instruments. For the FAST we make use of both archival and new spectra. The WHT data set contains only new spectra.

^bCheck mark if the spectra themselves are available.

^cCheck mark if the line and continuum fluxes are available.

correlations between X-ray, UV, and optical photometric bands on a time-scale of days–weeks, but interestingly found that X-ray to UV lags and UVW2 to U -band lags evolve with the luminosity state of the nucleus. In the case of the U -band lag, the authors suggest that the correlation with the luminosity state could be explained by a continuum-dependent contribution by the diffuse BLR gas to the continuum (Goat et al. 2019; Vincentelli et al. 2022). In X-rays, MKN 110 shows variability similar to other BLSy1, based on a comparison of their normalized excess variance (Ponti et al. 2012; Porquet et al. 2021). Recent VLBA observations also indicate the presence of variable 5 GHz radio emission, on time-scales of days–weeks, with the fastest varying emission originating within ~ 360 gravitational radii of the nucleus (Panessa et al. 2022, using a mass of $\log(M_{\text{BH}}/M_{\odot}) = 7.68^{+0.15}_{-0.23}$).

The series of spectroscopic RM papers (BK99, K01, K03b) produces an interesting and self-consistent story. The pole-on viewing angle would provide an explanation for the strong discrepancy between the mass estimates based on RM and those independent of the orientation of the BLR (K03b, Liu, Feng & Bai 2017), as most of the BLR motion would be perpendicular to our line of sight. However, a pole-on view cannot account for the lower mass estimate based on the stellar velocity dispersion (Ferrarese et al. 2001), which matches the RM results. A different potential counterindication is found in NGC 4051, in which a large He II velocity offset has been noted (Peterson et al. 2000). In this case, the offset is *to the blue*, which rules out gravitational redshift. Peterson et al. interpret the offset as the sign of an outflowing wind. We argue that although it is not required, it would be preferable if both blue and red offsets could be incorporated into a unified picture. A large part of the analysis presented in this paper will focus on the relation between the BELs and the ionizing continuum, however we will return to the discussion of black-hole mass and the nature of the offset of the broad and narrow emission lines in Sections 7 and 12.

3 DATA SETS USED IN THIS PAPER

Our data set consists of flux measurements from literature and of optical spectra drawn from a range of observing campaigns, including new observations. For those observations for which we have the spectrum available we use spectral fitting to calculate the line fluxes, as well as to extract information on the line profiles. An overview of our data and their provenance is given in Table 1. This table also includes information on the average observational parameters and conditions, where available. In total the sample consists of 207 spectral epochs spread over 28 yr (1987–2019). For 62 of the epochs the spectrum itself was used in our analysis. For the other 145 epochs,

referred to as the ‘literature data’ below, we only have measured fluxes available.

3.1 Literature data

The key studies of MKN 110 by BK99 and K01 provide line and continuum fluxes at a total of 49 epochs spread over 1987–2000. In this paper, we make use of the BK99 tabulated values for H α , H β , He I $\lambda 5876$, He II $\lambda 4686$, and the continuum flux at 5100 Å. The data set from the K01 paper is limited to one observing season (MJD 51480–51665). For these observations K01 provide continuum fluxes at 5100 Å, as well as at 4265 Å and 3750 Å for a subset of the epochs, and line fluxes for H α , H β , He II $\lambda 4686$, He I $\lambda 4471$, and He I $\lambda 5876$.

In addition to these published values, we make use of previously unpublished observations by B. Wilkes, J.P. Huchra, and B. Peterson. These observations were part of an RM campaign made using the FAST spectrograph (see below) in the period 1992–1996 (MJD 48651–50389). This campaign included MKN 110. The fluxes have not been published before now. From this archival FAST data set we have continuum fluxes at 5100 Å available, as well as line fluxes for H β and He II $\lambda 4686$. We will refer to this data set as WHP98.

3.2 Tillinghast (FAST) spectra

In the period 2002–2019 MKN 110 was observed 59 times by the FAST spectrograph on the Tillinghast 60 inch telescope at Mount Hopkins in Arizona (Fabricant et al. 1998). The first of these observations were part of a campaign undertaken by B. Wilkes, J.P. Huchra, and B. Peterson, concentrated into two observing seasons: 2002 November–2003 May and 2003 November–2004 May (MJD 52580–52760 and 52944–53126). These were high-cadence campaigns for RM (Note: this a separate campaign from the WHP98 data). Two further FAST spectra were part of studies reported by Landt et al. (2008, 2011). The FAST spectra taken in 2018 and 2019 were part of our monitoring programme.

The spectra were downloaded from the FAST public archive. The public FAST spectra have been reduced, including wavelength calibration, with the FAST reduction pipeline (Tokarz & Roll 1997). For inclusion in this study we flux calibrated the spectra. This calibration was performed using available FAST observations of standard stars. These observations were selected to match the target observation in time as closely as possible. The match in observing date lay within a week to a few weeks. We further applied a grey-shift to the FAST spectra, to correct for a possible offset in the flux calibrations between the FAST spectra and the other spectra in our sample. The correction is based on the assumed constancy of the

narrow [O III] λ 4959 and λ 5007 lines. The FAST spectra were scaled to match the [O III] fluxes of the SDSS spectrum.

3.3 SDSS spectrum

We use the Sloan Digital Sky Survey (SDSS) spectrum of MKN 110 taken in 2001. This is the only SDSS spectrum publicly available for MKN 110 (SDSS DR16). The SDSS observations and spectral reduction pipeline are discussed in Gunn et al. (2006) and Stoughton et al. (2002). No adjustments were made to the calibration of this spectrum. This spectrum is of particular importance in our data set, as the observation caught MKN 110 in an extremely low state, as we discuss in the following sections.

3.4 William Herschel telescope spectra

We observed MKN 110 on two occasions with the ISIS long-slit spectrograph on the 4.2m William Herschel telescope (WHT) on La Palma. The 5300 dichroic was used along with the R158B/R300B grating in the red/blue arms respectively, along with the GG495 order sorting filter in the red arm. This setup results in a spectral resolution of $R \sim 1500$ at 5200 \AA in the blue and $R \sim 1000$ at 7200 \AA in the red for a slit width of 1 arcsec.

The observations were carried out at parallactic angle. Cosmic rays were removed from the 2D spectra using the L.A.Cosmic method (van Dokkum, Bloom & Tewes 2012), after which we performed standard wavelength and flux calibrations. The flux calibration was performed with standard stars observed within 2 h of the observations and at similar airmass.

4 MEASUREMENTS OF FLUXES AND LINE PROFILES

For the FAST and WHT spectra we have made new measurements of both fluxes and line profiles. The fluxes were then combined with the fluxes from the BK99, K01, and P98 data sets, to make one combined flux data set covering the whole observational history of MKN 110. This data set is used for the analyses presented in Sections 5 and 6. The line profiles from the FAST and WHT spectra are used in Section 7 to study the BLR's kinematics.

4.1 Flux measurements

We measure the line fluxes for $H\alpha$, $H\beta$, He I λ 5876, He II λ 4686, He I λ 4471, and the continuum fluxes at 5100 \AA , 4652 \AA , and 3750 \AA . To match the BK99 and K01 data, we use the same method as described in BK99: the continuum flux is calculated as a local average and the line flux is calculated by defining a 'pseudo-continuum' at the position of the line. The pseudo-continuum is defined as the linear interpolation between two flux values, one either side of the line. This continuum level is then subtracted from the spectrum and the residuals are summed over a specified window for each line to estimate the line flux. To avoid being overly sensitive to fluctuations in a single wavelength bin, we define each of the two flux values by taking the median flux value over 20 wavelength bins and assigning this value to the central wavelength of the range of bins. Table 2 lists the spectral ranges over which the pseudo-continuum is calculated for the different lines species, as well as the spectral ranges that are summed over to find the line fluxes.

Our flux measurements are provided in Table 3. For completeness, we include all available values from the literature data in this table as well. We note that the pseudo-continuum method used to derive

Table 2. Overview of the wavelengths and spectral ranges used to calculate continuum and line flux values, using the pseudo-continuum method. This table follows Table 2 in K01.

Region of interest	Line window	Pseudo-continuum range
$H\alpha$	6400–6700 \AA	6260–6780 \AA
He I λ 5876	5785–6025 \AA	5650–6120 \AA
$H\beta$	4790–4940 \AA	4600–5130 \AA
He II λ 4686	4600–4790 \AA	4600–5130 \AA
5100 \AA continuum	–	5130–5140 \AA

these values produces a total line flux, which does not distinguish between broad and narrow line components. In Sections 5.2 and 6.2, we discuss our method for making corrections to the flux. The fluxes in Table 3 all represent the total line flux.

4.2 Line profiles

For the 62 epochs with available spectra (Table 1), we perform spectral fitting to extract detailed information about the observed changes in line profiles. We derive line widths and central wavelengths for different line components in He II 4686 and $H\beta$. The fitting is performed using the `lmfit` package.³For the Tillinghast spectra taken between MJD 52252 and 52798 and between MJD 52940 and 53140 the He II flux is so low that any information on the line profiles in the individual spectra is lost in the noise. In order to none the less extract information from this data set, we stacked these spectra and fitted the average 'low-state' spectrum. Those spectra with sufficient He II λ 4686 flux for a successful fit were modelled individually.

Through experimentation with the fitting window we find the optimal procedure is to fit the He II and $H\beta$ lines separately, in separate windows. The wavelength ranges for the windows are selected to split the problematic overlap region between He II and $H\beta$. For He II, the fitting region is set to 4400–4810 \AA (QSO restframe), and for $H\beta$ it is set to 4820–5050 \AA . Next, we test the effects of including a range of spectral model components: Gaussian or Lorentzian line profiles for He II, $H\beta$, [O III] λ 4959, and [O III] λ 5007, additional narrow line components for He II and $H\beta$, a power-law continuum of the form $A\nu^{-\alpha}$, and an optical Fe II emission template (Véron-Cetty, Joly & Véron 2004), convolved with a Gaussian kernel of variable width.

Our final fitting model is deliberately minimal. All many-component models had a strong tendency towards overfitting. An example of the results of our final fitting procedure for the two line species is shown in Fig. 1. The components included in the model for the He II region are the continuum power law and two Gaussians, for the broad and the narrow component of the line, respectively. The amplitude, width, and centre for the narrow line are fixed. The narrow line parameters are set to those derived in a free fit to the spectrum of MJD 53019, a high S/N FAST spectrum. The line flux and central wavelength of the He II narrow line in MKN 110 are therefore assumed to be constant during the time spanned by these observations, which is approximately 15 yr. For $H\beta$, the model consists of the same power law and four Gaussian components. The Gaussian components are used to model broad and narrow $H\beta$, [O III] λ 4959, and [O III] λ 5007. We list our fitting results for He II and $H\beta$ in Table 4.

³<https://lmfit.github.io/lmfit-py/>

Table 3. Overview of the flux data used in this paper, combining the results from multiple data sets. The full data set is available online.

MJD	F_{5100}^a	F_{4625}^a	F_{3750}^a	$H\alpha^b$	$H\beta^b$	$He\ II\ \lambda 4686^b$	$He\ I\ \lambda 4471^b$	$He\ I\ \lambda 5876^b$	Data set
46828.0	3.14 ± 0.09	3.97 ± 0.1	9.0 ± 0.2	1656.0 ± 24.0	477.9 ± 9.8	108.3 ± 5.2	30.8 ± 5.2	68.7 ± 5.4	BK99
47229.0	2.57 ± 0.08	2.83 ± 0.1	5.2 ± 0.2	1499.0 ± 22.0	389.3 ± 8.9	58.1 ± 4.2	20.6 ± 4.4	54.7 ± 4.7	BK99
47438.0	1.77 ± 0.07	1.96 ± 0.1	2.9 ± 0.4	1112.0 ± 18.0	287.3 ± 7.9	37.2 ± 3.7	17.6 ± 4.2	33.1 ± 3.7	BK99
47574.0	3.06 ± 0.09	3.53 ± 0.1	6.6 ± 0.4	1439.0 ± 21.0	347.0 ± 8.5	60.5 ± 4.2	26.7 ± 4.9	51.1 ± 4.6	BK99
47663.0	4.43 ± 0.12	5.27 ± 0.1	12.5 ± 0.4	1744.0 ± 24.0	475.1 ± 9.8	159.2 ± 6.2	25.8 ± 4.8	61.8 ± 5.1	BK99
47828.0	1.98 ± 0.07	1.99 ± 0.1	–	1520.0 ± 22.0	357.9 ± 8.6	30.6 ± 3.6	22.5 ± 4.6	41.7 ± 4.1	BK99
48651.8	5.68 ± 0.11	–	–	–	545.1 ± 10.9	153.2 ± 12.3	–	–	WHP98
48670.9	5.40 ± 0.25	–	–	–	581.2 ± 26.4	182.8 ± 14.6	–	–	WHP98
48676.8	5.04 ± 0.10	–	–	–	526.5 ± 10.5	129.5 ± 10.4	–	–	WHP98
48691.9	4.31 ± 0.09	–	–	–	529.4 ± 10.6	86.1 ± 6.9	–	–	WHP98

Notes. ^aunits of 10^{15} erg cm⁻² s⁻¹ Å⁻¹.

^b 10^{15} erg cm⁻² s⁻¹.

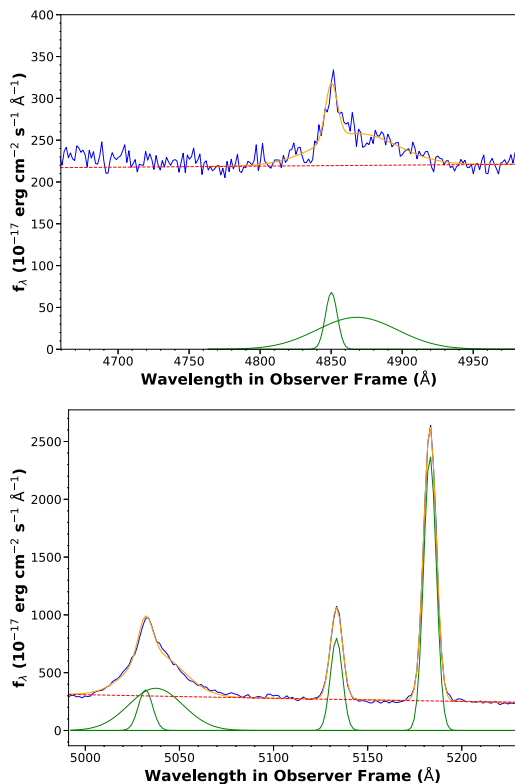


Figure 1. Example of the results of our fitting method for the two line species, as described in the text. The spectra were both taken with FAST. Top: The He II $\lambda 4686$ line fit (orange) containing the power-law continuum (dashed red) and two Gaussian components (green). The spectrum was taken on MJD 52997. Bottom: The H β line fit (colours as for He II), with power-law continuum and Gaussian line fits to narrow H β , broad H β , and the two [O III] lines. The spectrum was taken on MJD 53021.OK

5 HISTORY OF MKN 110 VARIABILITY

5.1 Evolution over three decades

Our data set includes 207 epochs spread over 28 yr and contains high-cadence and low-cadence periods of observation. Over this extended period of observation the flux at 5100 Å has shown variation by up to a factor of 9.4. We plot the long-term history of the optical continuum in Fig. 2. Over large parts of the light curve the variability appears stochastic, as would be expected for AGN (e.g. Kelly, Bechtold &

Siemiginowska 2009; Kozłowski et al. 2010). However, our sampling over much of the light curve is too sparse to capture shorter term changes. The inset in Fig. 2 shows a detailed look at the three high-cadence campaigns that took place over MJD 51544–53300. We have split the archival FAST spectra into the groupings FAST-RM1 and FAST-RM2, to mark the separate Reverberation Mapping campaigns. From the data in the inset we see that MKN 110 can undergo variations in flux up to a factor two during a single year. Over a single observing season the data show rising and falling trends on a time-scale of months.

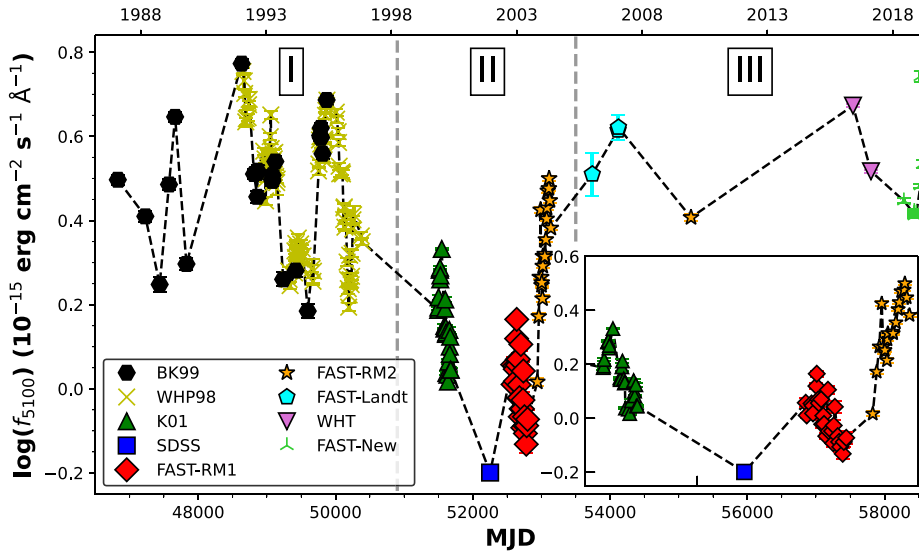
MKN 110’s strong photometric variability is accompanied by large changes in its optical spectrum. Fig. 3 shows a selection of spectra that cover the range of luminosity states. Over the course of the past decades, MKN 110 has shown large changes in its broad emission lines, in particular the broad Helium and Balmer lines. A more distant AGN, observed with lower signal-to-noise, showing the same variations might well have been labelled a Changing Look Quasar (e.g. LaMassa et al. 2015). The spectra also show that MKN 110 gets bluer when brighter, as is typical in AGN (Paltani & Courvoisier 1994). It is clear that while the BELs in MKN 110 change, they do not behave identically. The most striking aspect of the evolution visible in Fig. 3 is the extremely strong changes in He II $\lambda 4686$. In the lowest state (SDSS), broad He II is undetected. If we compare the next lowest state available to the maximum flux level, He II changes by a factor of 38. We also calculate the fractional variability (F_{var} ; cf. Vaughan et al. 2003) over the full time range of our data. We find F_{var} of 0.460 ± 0.002 for the 5100 Å continuum flux, 0.338 ± 0.001 for H α , 0.367 ± 0.002 for H β , and 0.694 ± 0.006 and 0.698 ± 0.020 for He II $\lambda 4686$ and He I $\lambda 5876$, respectively. We will investigate this remarkable differential behaviour of the various line species. In the rest of this section we detail how we prepare our data set for this analysis.

5.2 Corrections to the flux data

To present a uniform data set, we make a number of corrections to our flux data. The first is to compensate for the narrow-line contribution to the He II $\lambda 4686$ fluxes. The pseudo-continuum method we have used to measure the line fluxes does not distinguish between the broad and narrow components of a line. It simply returns all the emission above the continuum level in a given interval (Section 4.1). As we wish to investigate the behaviour of the broad emission lines, we require a correction for the emission from the Narrow Line Region (NLR). Although it is possible to model the broad and narrow components separately through spectral fitting, we do not have the spectra available for the literature data sets. We therefore require a more general method of correction. Visual inspection of

Table 4. The results of our spectral fitting of the He II $\lambda 4686$ and H β lines. The full data set is available online.

MJD	λ_c^a	He II $\lambda 4686_{\text{broad}}$ flux ^b	σ^a	λ_c^a	H β_{broad} flux ^b	σ^a	H β_{narrow} λ_c^a
52961	4878.21 ± 2.39	19.12 ± 2.19	28.07 ± 2.80	5040.26 ± 0.51	89.35 ± 4.14	16.27 ± 0.64	5032.21 ± 0.03
52975	4872.73 ± 1.74	25.65 ± 2.03	29.31 ± 2.03	5038.91 ± 0.39	110.57 ± 3.96	14.97 ± 0.47	5031.97 ± 0.03
52988	4873.81 ± 9.15	31.08 ± 13.23	43.79 ± 12.75	5037.80 ± 0.49	97.56 ± 4.73	13.67 ± 0.58	5031.99 ± 0.04
52997	4869.03 ± 1.59	24.95 ± 1.85	26.71 ± 1.80	5038.53 ± 0.30	137.97 ± 3.78	14.26 ± 0.35	5032.59 ± 0.04
53001	4866.63 ± 2.22	24.98 ± 2.39	31.90 ± 2.63	5037.66 ± 0.26	154.69 ± 3.75	14.07 ± 0.31	5032.04 ± 0.03
53005	4866.26 ± 2.19	18.02 ± 1.99	22.97 ± 2.41	5037.25 ± 0.26	151.16 ± 3.67	14.52 ± 0.31	5031.76 ± 0.03
53016	4873.31 ± 4.87	7.33 ± 2.00	20.45 ± 5.38	5037.53 ± 0.30	138.93 ± 3.96	14.74 ± 0.37	5031.60 ± 0.03
53019	4872.98 ± 2.30	14.23 ± 1.63	24.12 ± 2.56	5036.64 ± 0.25	142.73 ± 3.32	14.01 ± 0.30	5031.56 ± 0.03
53021	4873.52 ± 2.47	24.07 ± 2.65	27.64 ± 2.92	5037.42 ± 0.29	131.99 ± 3.65	14.42 ± 0.35	5031.96 ± 0.03
53047	4869.94 ± 2.43	21.10 ± 2.46	25.40 ± 2.73	5037.78 ± 0.27	167.45 ± 4.19	14.53 ± 0.33	5032.55 ± 0.03
53049	4868.07 ± 2.76	27.03 ± 3.22	33.32 ± 3.34	5037.27 ± 0.27	172.79 ± 4.40	14.44 ± 0.33	5031.99 ± 0.03

Notes. ^aunits of Å.^bunits of 10^{15} erg cm⁻² s⁻¹.**Figure 2.** The long-term continuum light curve for MKN 110 based on spectrophotometric fluxes at 5100 Å (f_{5100}). The AGN shows significant variability in its output, including multi-year trends, as well as seemingly more erratic jumps. MKN 110 reached a low state around the time of the SDSS spectral observation. The epochs have been labelled according to the origin of the spectral data, with the abbreviations as listed in Table 1. The archival FAST spectra have been divided into RM1 and RM2, representing two separate Reverberation Mapping campaigns. The Roman numerals and dashed grey lines indicate the three observational epochs we define in our data set (see Section 6.4). The inset shows a closer view of the observational epochs for the high cadence K01, FAST-RM1, and FAST-RM2 data. These RM data show that MKN 110 continued to display low-level variability in addition to the larger structural flux changes.

the He II $\lambda 4686$ line (Fig. 3) shows that the He II narrow component is quite distinct. The low-state SDSS spectrum, in which the broad component has vanished, contains a clear narrow He II component.

We therefore assume the narrow He II component to be constant over our period of investigation. We note there is evidence for variability of the [O III] narrow lines in NGC 5548 on a time-scale of decades, significantly longer than the broad line response time-scale (Peterson et al. 2013). We are not able to exclude such narrow-line variability from our data set, which may therefore introduce an additional uncertainty in the He II broad component fluxes. This is taken into account when we estimate the total uncertainty in the line fluxes in Section 6.3. We measure the flux of narrow He II $\lambda 4686$ in the SDSS spectrum, fitting a single Gaussian to the line. Our correction to the He II flux data consists of subtracting the flux of the narrow component in all epochs, giving us an estimate of the broad-line flux. For the other line species (H α , H β , and He I $\lambda 5876$) there is no epoch in which the broad component is completely gone.

We will correct these fluxes using a different method than for He II. As this other method requires us to first evaluate the response of the various line species to the changing luminosity state, we will cover this step later on, in Section 6.2.

We next adjust the data to account for the BLR's spatial stratification. RM results show that a fluctuation in the FUV flux originating in the central engine will reach the line-forming regions of different line species at different times. Representing the fluxes from the same observational epoch as synchronous measurements implicitly assumes that the line-forming regions are affected by the same ionizing flux. This approach would therefore ignore light traveltimes between the different regions of the stratified BLR. In the subset of our data set consisting of fluxes from RM studies (K01, FAST-RM1, and FAST-RM2) we are able to correct for this effect, as the cadence of observations is sufficiently high.

We make use of the lags reported in K01 (Table 5). The date of each flux observation is shifted by the appropriate lag, after which the

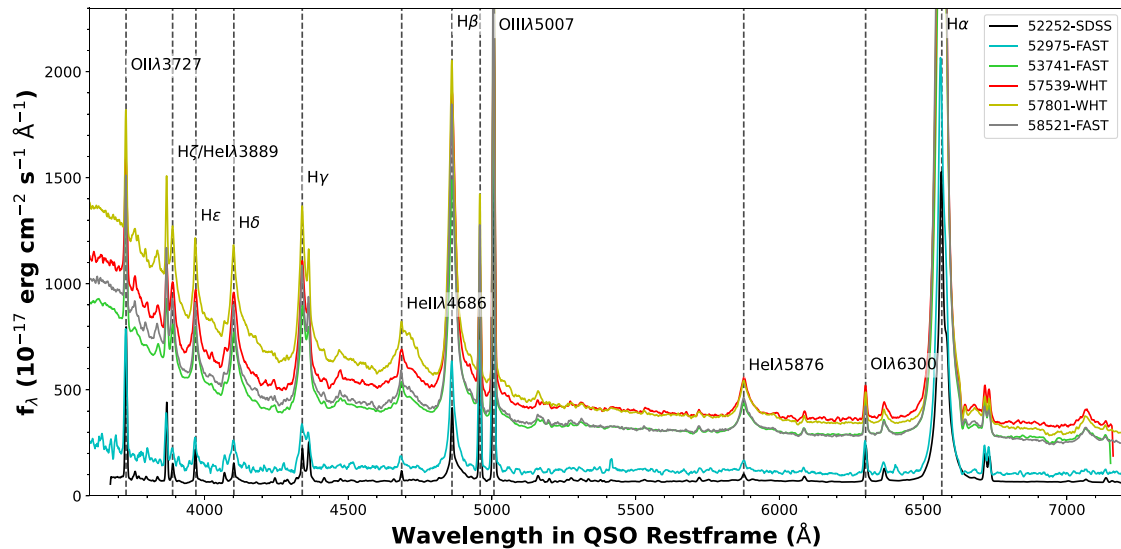


Figure 3. A selection of redshift-corrected spectra from high, low, and intermediate luminosity states of MKN 110. The spectra show an evolving blue continuum as well as strong variability in the BELs. We have marked some of the most important emission lines in the plot. Particularly noteworthy is the variability in the broad He II $\lambda 4686$ line, which is not detected in the SDSS spectrum, is very strong and broad in the WHT spectrum of MJD 57539, and is in intermediate states at other epochs.

Table 5. Fitting results long-term BLR responsivity curves.

Line	σ_{est}^a	a^b	y_{sat}^c	RM lag d
H α	0.15	$0.39^{+0.06}_{-0.04}$	$0.65^{+0.09}_{-0.08}$	$32.3^{+4.3}_{-4.9}$
H β	0.18	$0.57^{+0.04}_{-0.06}$	$0.90^{+0.10}_{-0.06}$	$24.2^{+3.7}_{-3.3}$
He I $\lambda 5876$	0.24	$0.79^{+0.07}_{-0.07}$	$1.47^{+0.16}_{-0.15}$	$10.7^{+8.0}_{-6.0}$

Notes. ^aEstimated uncertainty (normalized line flux).

^bBest-fitting value for the slope of the two-component function.

^cBest-fitting value for the saturation level of the two-component function.

^dReverberation Mapping lags presented in K01 (days).

fluxes are matched with the closest, lag-corrected 5100 \AA continuum fluxes. We performed all analyses presented in this paper with the lag-corrected and the original data set and find no significant changes in our conclusions. We are therefore confident that the inability to correct for lags among the lower cadence data sets has no significant impact on our results.

In the final step of our corrections, the fluxes are normalized. We normalize to the fluxes from a single epoch. The normalization allows for the investigation of the relative change in line-flux. The fluxes used for the normalization are those from the observation on MJD 47574, an epoch from the BK99 data set.⁴ All fluxes at this epoch therefore have a value of unity in our data set, while fluxes at other epochs are scaled relative to the flux on this date.

To summarize the various changes we make to the data set: we have corrected the He II $\lambda 4686$ fluxes by fitting the flux of the narrow component (assumed to be constant) and subtracting it. We have adjusted (where possible) the combination of line-flux and continuum-flux measurements, to compensate for the light traveltime between different line forming regions in the BLR. And finally, we normalized all flux values to the measurements on one particular date: MJD 47574.

⁴The choice of date is arbitrary for our normalization.

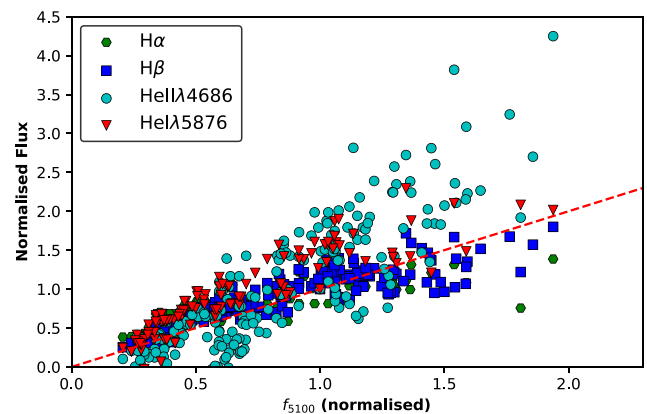


Figure 4. The fluxes of four broad-line species in MKN 110. The line fluxes are plotted against the continuum flux at 5100 \AA . The line-species are H α (green hexagons), H β (dark blue squares), He II $\lambda 4686$ (cyan circles), and He I $\lambda 5876$ (red triangles). All fluxes have been adjusted as specified in Section 5. The red dashed line indicates a 1:1 ratio between the line and continuum fluxes. The He II $\lambda 4686$ flux has a distinct responsiveness compared to the other lines: it increases more rapidly than the optical continuum and continues to grow in flux at higher f_{5100} , whereas the response of the other line species appears to flatten.

5.3 The connection between emission lines and continuum flux

The corrected and normalized fluxes are shown in Fig. 4, where we plot the line fluxes against the optical continuum at 5100 \AA . The 5100 \AA flux is often used in reverberation studies as a proxy for the driving continuum, as this region of the spectrum is relatively free of contamination by blended lines and is more readily accessible to observations than the UV continuum (Peterson et al. 1992). All line species in Fig. 4 show a clear flux correlation with the continuum, as would be expected. As the optical continuum flux increases, the ionizing flux powering the BLR increases as well. We also note a

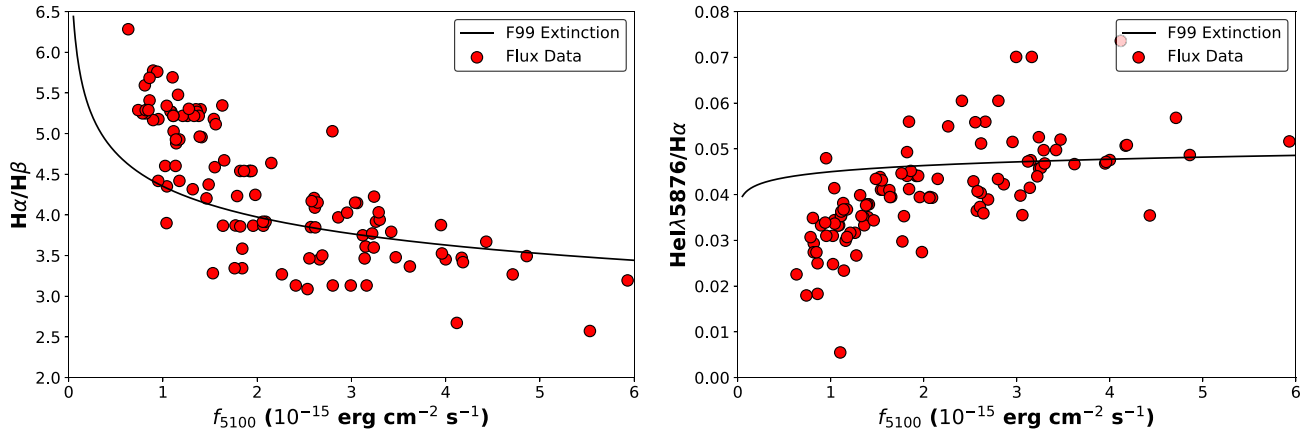


Figure 5. The line flux ratios $H\alpha/H\beta$ (left-hand panel) and $He\ I\ \lambda 5876/H\alpha$ (right-hand panel) are plotted against the 5100 Å continuum flux. We use these metrics to investigate whether variable obscuration can explain the spectral evolution observed in MKN 110. The theoretical reddening curve is calculated using the extinction curve from Fitzpatrick (1999, F99) under the assumption that all changes in continuum flux are due to dust reddening. The data and theoretical extinction are a poor match. We therefore rule out a changing attenuation by dust as the driving force for the observed variability in the line and continuum flux levels. It appears that these changes are instead driven by changes in the ionizing power source.

strong differentiation in response among the line species, with the Balmer lines having the flattest response, $He\ II\ \lambda 4686$ varying *with a greater amplitude than the optical continuum*, and $He\ I\ \lambda 5876$ being intermediate. The slope of the response of the Balmer lines is close to 1:1 with the optical continuum (as indicated by the dashed red line) and shows signs of an even lower response at higher continuum fluxes. In contrast, the $He\ II$ line shows no sign of flattening off at high luminosity states.

5.4 Ruling out reddening

We consider whether the detected flux variations can be explained by variable obscuration by intervening dust. To check for reddening we use the line flux ratios $H\alpha/H\beta$ and $He\ I\ \lambda 5876/H\alpha$, viewed against the 5100 Å continuum flux. The dust is modelled as a single sheet and we make use of the extinction curve from Fitzpatrick (1999). We calculate the level of reddening required to explain the relative change in the 5100 Å flux and model the expected value for the given line ratios. The comparison is shown in Fig. 5. The reddening modelled for $H\alpha/H\beta$ (left-hand panel) shows the same overall behaviour as the data, but still provides a poor fit: it does not match either the relative constancy of the ratio at high luminosities, or the steep rate of change at low luminosities. The ratio of $He\ I/H\alpha$ (right-hand panel) shows an even poorer fit. Thus, we find that variable, single-screen extinction due to dust does not dominate the variability in line and continuum. It therefore appears likely that the variability in the line fluxes is indeed attributable to changes in the ionizing flux, and subsequent reprocessing in the BLR.

6 THE RESPONSE OF THE BLR IN MKN 110

6.1 Using $He\ II\ \lambda 4686$ as an FUV continuum proxy

The Balmer and Helium emission lines discussed in this paper are all recombination lines, powered by an ionizing ($E > 13.6\text{ eV}$; FUV) continuum, which we cannot observe directly. Based on the strength of emission lines compared to the observed continuum, it has long been suspected that the continuum powering the broad-line emission, the emission the BLR ‘sees’, is different from the

continuum that we can observe directly (Mathews & Ferland 1987; Korista, Ferland & Baldwin 1997). This has motivated observational studies to approximate the unseen part of the SED, using broad emission lines (Mathews & Ferland 1987; Meléndez et al. 2011; Panda et al. 2019; Ferland et al. 2020). Modelling of AGN SEDs, bound by the constraints provided by observational studies, also shows a limited connection between the optical continuum (f_{5100}) and the FUV (Done et al. 2012; Jin, Ward & Done 2012; Kubota & Done 2018). As the optical region of the SED lies significantly redwards of the peak in the spectrum, the FUV flux can take on a wide range of values, with only marginal changes in the optical flux (Kubota & Done 2018; Ferland et al. 2020). Reverberation studies have also observed a negative correlation between wavelength and variability amplitude (e.g. Fausnaugh et al. 2016), which is evident in MKN 110 (Vincentelli et al. 2021). The f_{5100} flux is therefore a useful measure to detect *when* the FUV continuum changes, however it is less suitable to measure *how much*. For the latter, the broad emission lines provide a better approach.

The $He\ III$ recombination lines in AGN, such as $He\ II\ \lambda 4686$, are powered by photons with an energy greater than 54.4 eV. This means $He\ II$ lines provide a measure of the continuum flux in the FUV part of the SED, even beyond the H-ionizing region (Korista et al. 1997). Ferland et al. (2020) argue for the use of $He\ II\ \lambda 4686$ in particular, as a relatively clean metric for the strength of the FUV continuum. Based on photoionization modelling, Eastman & MacAlpine (1985) found that in BLR conditions, photons for $He\ II$ resonance lines, in particular $He\ II\ Ly\ \alpha$, have a high probability of being absorbed by H I. This means that, unlike the Balmer lines, which are affected by several complicating factors, $He\ II$ recombination is in good approximation to Case B for Hydrogen⁵ (Ferland et al. 2020). $He\ II\ \lambda 4686$ therefore functions as an FUV photon counter: it provides our most direct measurement of the strength of the ionizing continuum. The fact that in MKN 110 we observe the $He\ II$ flux to show *larger* variations than the optical continuum agrees with this idea. In the following we will therefore explore the use of the $He\ II\ \lambda 4686$ flux as a proxy for the FUV ionizing continuum of MKN 110.

⁵In Hydrogen Case B recombination, the ionized gas is assumed to be optically thin at photon energies below the Lyman limit.

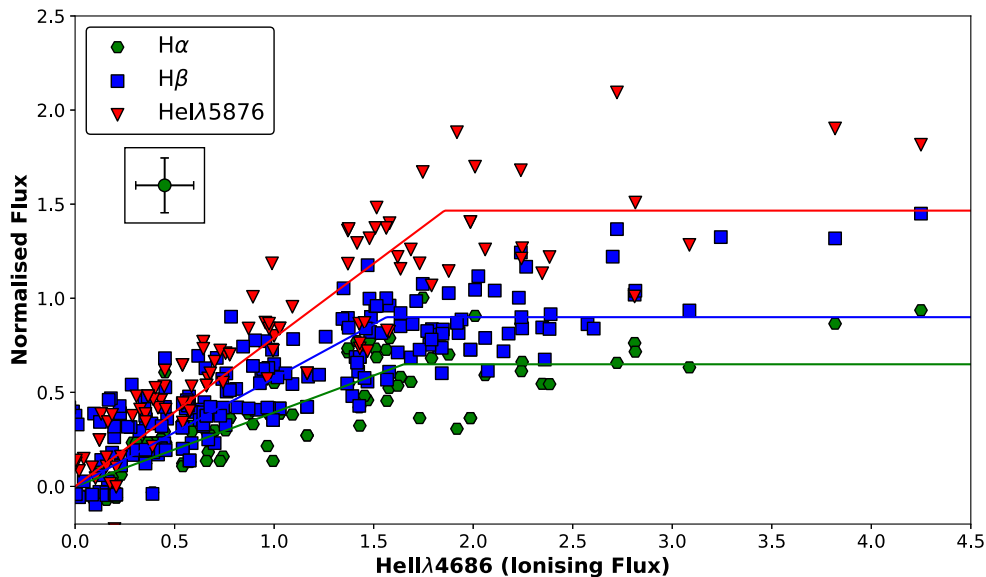


Figure 6. The normalized line fluxes for $H\alpha$ (green hexagons), $H\beta$ (blue squares), and $He\text{ I } \lambda 5876$ (red triangles), plotted against the normalized $He\text{ II } \lambda 4686$ flux. All line fluxes have been corrected by adjusting for the non-variable narrow-line component (see Sections 5.2 and 6.2). The responses of the line fluxes have been modelled using a two-component fitting function. The fitting results show the line species have different gradients in their response, as well as different saturation levels. This stratification indicates slope and saturation level are efficient parameters for distinguishing the three lines species. The uncertainties on the data were calculated by incorporating the intrinsic scatter apparent in the data (see Section 6.3). We include the uncertainties on the data set for $H\alpha$ as an example, in the top left of the plot.

6.2 Correcting for the non-responsive flux component

Fig. 6 shows normalized $H\alpha$, $H\beta$, and $He\text{ I } \lambda 5876$ plotted against $He\text{ II } \lambda 4686$. The fluxes for the three lower ionization lines have been corrected for the presence of a non-varying component in the following way. Each line species showed a vertical offset, indicating that at the lowest $He\text{ II } \lambda 4686$ flux states, there was still a measurable line flux. This is despite the fact that at the lowest flux state (associated with the SDSS spectrum), the $He\text{ II } \lambda 4686$ flux had completely disappeared. We correct the fluxes by removing this non-variable component, as our interest is in the fraction of the flux that is responsive to $He\text{ II}$ changes. Unlike for $He\text{ II } \lambda 4686$, we have not subtracted a narrow line flux from the broad component for $H\alpha$, $H\beta$, and $He\text{ I } \lambda 5876$ (Section 5.2). This means that the non-varying component in these lines must at least partially be associated with narrow line emission. However, it will also include any non-varying broad-line flux.

The correction for the non-varying flux contribution is made by performing a linear fit to the flux data for each line species in the range where normalized $f_{He\text{ II}} < 1$. The offset of the data is such that it requires the linear fit to pass through the origin (see Fig. 6 for the effect in the corrected data set). The downward shifts in units of normalized flux are 0.2, 0.35, and 0.45 for $He\text{ I } \lambda 5876$, $H\beta$, and $H\alpha$, respectively.

6.3 Quantifying the response

It is evident from Fig. 6 that, above a threshold, the fluxes of all three line species, $H\alpha$, $H\beta$, and $He\text{ I } \lambda 5876$, have a diminishing response to an increase in $He\text{ II } \lambda 4686$ flux. For the highest $He\text{ II}$ fluxes the response appears almost flat. Each line species responds approximately linearly at low luminosities and saturates to a fixed maximum flux as the $He\text{ II}$ line increases further. There are also notable differences among the line species: both the gradient of the response at low $He\text{ II}$ fluxes and the saturation level of the fluxes

increases from $H\alpha$ and $H\beta$ to $He\text{ I}$. A diminishing line response was also noted for the $C\text{ IV } \lambda 1550$ line compared to the 1350 Å continuum (Wamsteker & Colina 1986). And similar behaviour was described by Ferland et al. (2020) for the $He\text{ II } \lambda 4686$ line itself. Using a low-redshift AGN sample spanning a very large range in luminosity, Ferland et al. (2020) showed that the highest luminosity sources, identified mainly with NLSy1s, showed the largest deficit in $He\text{ II}$ emission, relative to predictions based on the SED.

To quantify the observed behaviour, we fit the flux data with a simple empirical function. We experimented with a number of functions and found that a double straight line results in the most stable fits whilst also capturing the two key aspects of the response: a difference in gradient at low $He\text{ II}$ fluxes and a difference in saturation level. If we let y represent the normalized line flux for each of the the low-ionization lines and x the line flux for normalized $He\text{ II } \lambda 4686$, our fitting function has the form

$$y(x) = \begin{cases} ax & \text{if } x \leq x_k \\ y_{\text{sat}} & \text{if } x > x_k. \end{cases} \quad (1)$$

Here x_k represents the ‘knee’ value of the $He\text{ II}$ flux, where $y(x_k) = y_{\text{sat}}$, i.e. the turning point in the response. The free parameters are the slope a and the saturation level y_{sat} , with x_k fixed by the other two parameters.

To find the uncertainties on our fits, we need to account for the uncertainties in our data set. We note that the measurement uncertainties, associated with the statistical uncertainties of the spectral fits at each epoch, represent an underestimate of the real variance. We are interested in the gradual, long-term evolution of MKN 110, which means that the uncertainties of interest are a combination of the measurement uncertainties and the scatter around the long-term behaviour caused by short-term (days–months) changes in the line-forming regions. We find that this scatter, evident in Fig. 6, is the dominant cause of uncertainty in our data set. To estimate the level of uncertainty, we first fit our model function using

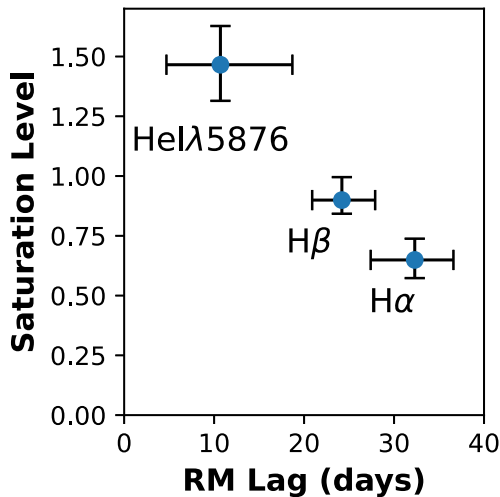


Figure 7. The saturation levels (y_{sat}) for H α , H β , and He I $\lambda 5876$, plotted against the Reverberation Mapping lags for these line species presented in K01. The saturation levels belong to the two-component model for the response of the normalized line fluxes to changes in the He II $\lambda 4686$ flux (Section 6.3). The results show a strong negative correlation between an emission line’s ability to track the continuum and the distance of the line-forming region from MKN 110’s central engine.

the statistical errors of the data. We then apply the standard deviation of the residuals as a uniform error on the data set (for each line species separately). We then use this new error estimate, which now includes the additional uncertainties associated with short-term variability, to calculate the best-fitting parameters of our fitting model. The results of our fits, as well as the estimated 2σ uncertainties, are listed in Table 5 and the best-fitting models are included in Fig. 6.

The response results show an interesting anticorrelation when combined with the measured lags from the K01 RM study. These lags represent the approximate response time of each line species to changes in the FUV continuum and are therefore directly related to the distances between the SMBH and the different line forming regions. We plot our values of y_{sat} against the RM lags in Fig. 7. He I $\lambda 5876$, which is formed closer to the central engine, saturates at a higher level than the other two lines. Similarly H β saturates at a higher level than H α . The ability of a line species to track the increasing FUV continuum therefore appears closely related to the physical parameters that determine the optimal line-forming distance from the SMBH. This conclusion can be drawn without making any assumptions about the nature of these physical parameters: we only need to assume that the RM lag corresponds to the distance from the central source of ionizing radiation.

6.4 Responsivity from epoch to epoch

To estimate the uncertainties on our line-responsivity fits (Fig. 6) we made the assumption that a combination of short-term variability and measurement uncertainties led to a random scatter around a single long-term response curve. This approach allows us to treat all the spectroscopic data, which cover over 30 yr, as a single data set. Given the time-span of the combined data set, we now investigate whether a trend is visible on time-scales of several years. Over the three decades of observations, MKN 110 varies from high to low luminosity states. When MKN 110 returns to a luminosity state that it was previously in, do the line fluxes return to the same level they had before? If not, is this a form of hysteresis, in which the AGN ‘remembers’ its

evolution over several years? To answer these questions, we consider the difference in responsivity among different observational epochs. We define three such periods (see Fig. 2):

- (i) MJD 46900–50900, covering BK99 and WHP98.
- (ii) MJD 51500–52300, covering K01, FAST-RM, and SDSS.
- (iii) MJD 53700–58500, new FAST and WHT data.

In the first and last epochs, MKN 110 is on average in a higher flux state than during the middle epoch, in which MKN 110 dims to the overall lowest state (SDSS). Although the cadence of the spectroscopic coverage in epochs I and III is not as high as in epoch II, it is unlikely that all of our observations will have missed historic low states. To explore whether the long-term evolution of the luminosity state, from epoch to epoch, leaves a detectable imprint on the BLR and the line responsivities, we consider the response curves for each of the line species separately.

In Fig. 8 we show the example of H β (plotted against He II as in Fig. 6), where the data have now been grouped by epoch. He I $\lambda 5876$ and H α show similar patterns as H β . The data from epoch I show a shallower response than those of epoch II. As the data in epoch II and III do not cover a sufficiently broad range in normalized He II flux, we compare the responsivity among epochs using a simple linear regression. The results of the linear fits for the three line species are listed in Table 6. The fitting results confirm the change in response over time: we measure a significantly steeper responsivity for epoch II as well as a difference in slope between epoch I and III. The stronger response for epoch II is as expected, as this epoch is dominated by low flux-state data points (the sloped part in our two-component model). The difference in slope between epoch I and epoch III suggests that the responsivity does not only evolve with flux state, but also over time-scales of 5–10 yr.

The data sets comprising epoch II provide our most detailed view of the evolution of continuum and BLR in MKN 110. We examined whether there is any significant difference among the different seasons within this middle epoch, which cover shorter periods (up to 1 yr) of rising or lowering continuum levels. Linear regressions on subsets of the data show that the slopes are all consistent within uncertainties. It therefore appears that the BLR responsivity changes only on longer time-scales. In general, responsivity of the BLR to changes in ionizing continuum will be due to either lighting up different parts of a static but distributed structure, or to the BLR physically changing. The fact that we see repeatability on short time-scales but differences on long time-scales suggests that in fact *both* of these effects are happening. We will return to this point in Sections 10 and 11.

7 LINE PROFILES AND KINEMATIC EVOLUTION

The broad components of the emission lines in MKN 110 are redshifted by velocities of 100s to 1000s km s $^{-1}$, relative to their narrow-line components and therefore relative to the redshift of the AGN and its host. This broad-to-narrow-line offset is most distinct for He II $\lambda 4686$, but is also visible as a line asymmetry in the Balmer lines (Fig. 1). As noted in Section 2, the offset has been associated with a gravitational redshift (K03b). However, the large range among different mass estimates for the SMBH in MKN 110 leads us to investigate alternatives. We first consider whether the offset in the emission lines, like the line flux, depends on the level of the FUV ionizing continuum. We focus on two lines: He II $\lambda 4686$ and H β . As we are investigating changes in the offset over time, we follow the fitting procedure set out in Section 4.2 (in contrast to the procedure

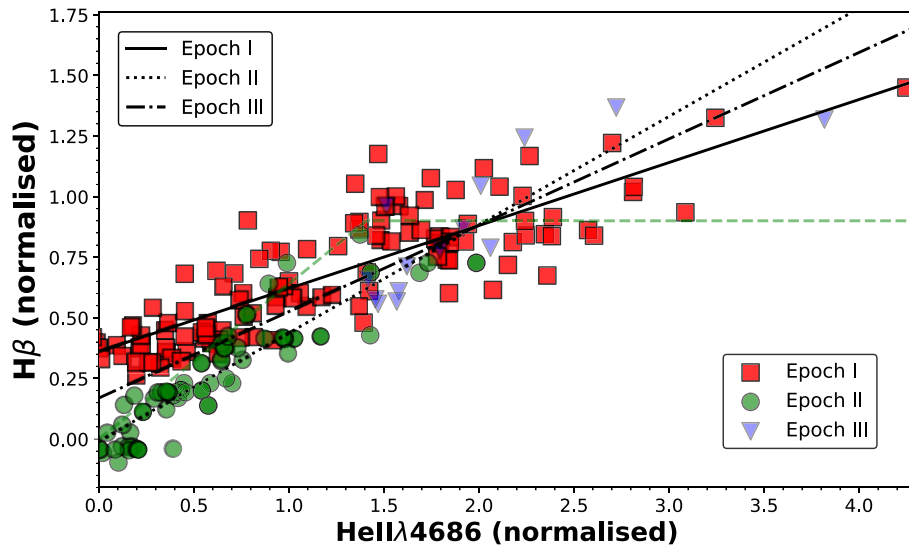


Figure 8. The normalized $H\beta$ flux data plotted against $\text{He II } \lambda 4686$, split according to epoch as in Fig. 2. The dashed green line is our best-fitting two-component model for the full $H\beta$ data set as seen in Fig. 6. The three straight lines represent the results of linear regressions on subsets of the data: continuous, dotted, and dot-dashed lines for epochs I, II, and III, respectively. It is noticeable that the slope in the data points for the second epoch, associated with a relatively low state, is different from those of the two ‘high state’ epochs. This implies that identical changes in He II flux resulted in different changes in $H\beta$ flux, with a time interval of 5–10 yr, from one epoch to the next (see Fig. 2). On shorter time-scales, within a single epoch, this effect is not visible (Section 6.4). The slopes of the linear regressions indicate that there is also a difference in response between the two high-state epochs.

Table 6. Results of a linear regression of the normalized line flux data, separated by line species and by epoch.

Line	Full Shift ^a	Slope	I Offset	R^{2b}	Slope	II Offset	R^2	Slope	III Offset	R^2
$H\alpha$	0.45	0.10 ± 0.04	0.46 ± 0.08	0.26	0.27 ± 0.03	0.04 ± 0.02	0.60	0.13 ± 0.07	0.37 ± 0.14	0.23
$H\beta$	0.35	0.26 ± 0.02	0.36 ± 0.02	0.71	0.45 ± 0.02	-0.01 ± 0.02	0.83	0.36 ± 0.07	0.17 ± 0.15	0.67
$\text{He I } \lambda 5876$	0.20	0.26 ± 0.06	0.69 ± 0.12	0.48	0.65 ± 0.04	0.13 ± 0.03	0.80	0.48 ± 0.14	0.40 ± 0.29	0.49

Notes. ^aShifts applied to the normalized line fluxes (Section 6.2).

^bCoefficient of determination ($1 - \sum(\text{residuals})^2 / \text{Variance}$).

in K03b, who use the MAD spectrum). The large amount of available spectra in our data set allows us to track the line evolution over time.

7.1 Offset, FUV flux, and line width

The data set used for this part of the study contains all FAST and WHT spectra. As discussed in Section 4, the lowest state spectra are not included individually. These spectra are included as an average, established by stacking the spectra, such that they have sufficient S/N for spectral fitting. All spectra in FAST-RM1 as well as the first spectrum of FAST-RM2 (MJD 52940) are stacked together. The other spectra are fit individually. Before comparing the narrow line to broad line offset, we confirm that the narrow line components of He II and $H\beta$ are found at the same redshift. For He II , the centre of the narrow line was kept fixed in the fitting procedure (Section 4.2), at a value corresponding to $z = 0.0351$. For $H\beta$, we find that the median value of the narrow line centre, over all fitted spectra, also corresponds to $z = 0.0351$. The standard deviation of the $H\beta$ narrow-line centres is $\sim 0.5 \text{ \AA}$, corresponding to around 28 km s^{-1} . This difference is very small compared to the measured offsets between narrow and broad components. In addition to the similarity in redshifts, we find that the width (σ) of the narrow-line components is comparable within 10 per cent: 4.2 \AA for He II and 3.8 \AA for $H\beta$. We therefore conclude

that the narrow-line components for He II and $H\beta$ are formed in the same part of the Narrow Line Region and can be reliably used to gauge the offsets of the broad line components.

The results of our spectral fitting indicate that the velocity redshift of broad-line components compared to the narrow lines changes significantly over time, for both He II and $H\beta$. The correlations among offset and $\text{He II}/\text{FUV}$ flux present a complex picture of MKN 110’s broad-line variability. Fig. 9 shows the velocity offset between components plotted against broad He II flux. The left-hand panel shows the results for He II and the right-hand panel the results for $H\beta$. The data have been split between the FAST-RM2 data (red circles) and the newer FAST and WHT data (blue squares). The epoch is indicated by the shading of the colours, going from light to dark for later epochs. In the $H\beta$ plot, one can trace the passage of time from the top left-hand side (light red circles) to the bottom right-hand side (dark blue squares). The observed increase in He II flux agrees with the rise in the continuum light curve for this period (See epochs II and III in Fig. 2).

The first thing to note in Fig. 9 is that the average offset for He II is significantly larger than for $H\beta$. Secondly, $H\beta$ appears to have a negative correlation between He II flux and offset: as the He II line flux increases, the offset becomes smaller. In other words: as the ionizing flux goes up, the relative redshift of the broad component

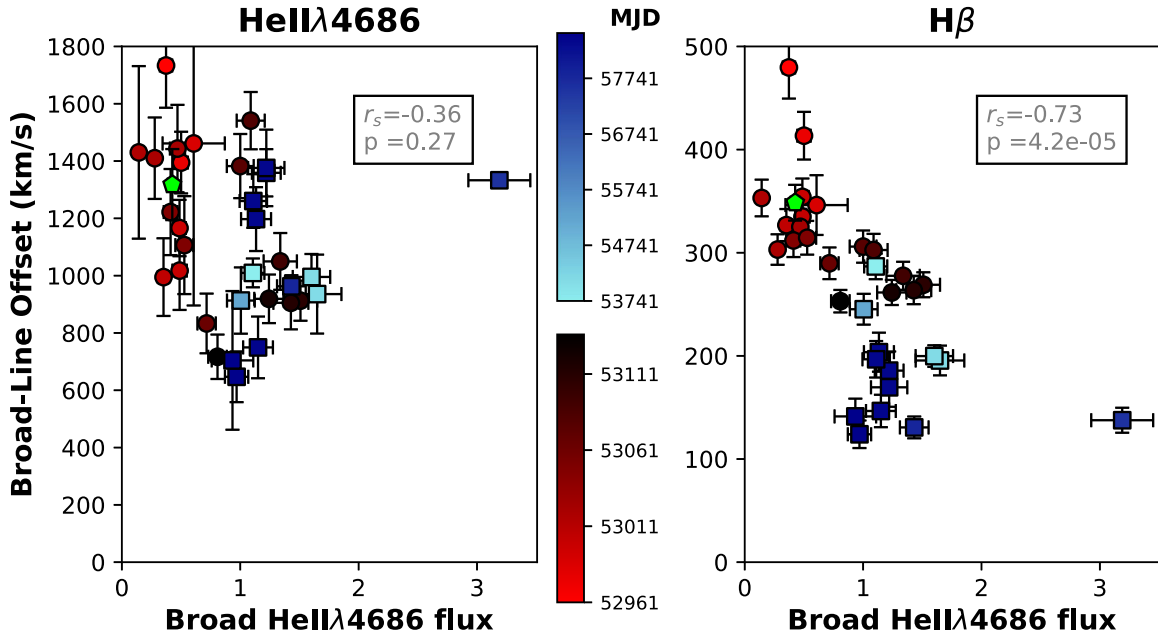


Figure 9. The offset between the line centres of the broad and narrow components of He II $\lambda 4686$ (left-hand panel) and H β (right-hand panel), plotted against the normalized broad He II flux. The offset between between the broad and narrow lines measures the relative redshift of the broad line components. The broad He II flux acts as a proxy for the ionizing continuum. The shading of the colours indicates the time at which the spectrum for the data points was taken. The two colour ranges represent the observational periods: red circles cover the spectra of the FAST-RM2 campaign (MJD 52961–53137) and blue squares cover the newer FAST and WHT spectra (MJD 53741–58500). The green hexagon represents the fits from the stacked ‘low-state’ FAST spectra (MJD 52252–52798). r_s is the Spearman ranked correlation coefficient. The p value is for a two-tailed test (on a null hypothesis of non-correlation) of Pearson’s correlation coefficient and it indicates the probability that the two parameters are not correlated. Both r_s and the p -value relate to the the full data-sets. The He II data show two distinct ‘branches’ as the ionizing flux changes over time, whereas H β shows a consistent correlation.

goes down. The correlation for H β is consistent over the different epochs, whereas the He II behaviour is less straightforward, as it appears to form two distinct branches. Finally, we note that not just the *average* offset, but the *change* in offset is larger for He II than for H β . The somewhat aberrant high He II flux point in the far right of both plots is associated with the WHT spectrum of MJD 57539, the spectrum with the highest S/N in the sample.

We next consider the correlation between the broad-line widths and the He II $\lambda 4686$ flux. The results are shown in Fig. 10. The line widths for He II are significantly larger than for H β , in agreement with the notion that He II is formed closer to the ionizing source (as found in RM studies). A luminosity-dependent line width, as would be the case for a ‘breathing’ BLR, is evident for H β . In agreement with the results shown in Fig. 9, the distance of the broad-H β emitting region to the SMBH (which is inversely correlated with the broad-line width) increases with luminosity. This breathing of the BLR is expected, if the BLR motion is Keplerian. This comparison functions as a check on both our line-fitting results and the basic assumptions made in the analysis presented so far. Remarkably, He II shows the opposite trend. As was the case in the offset-versus-flux results, the data for H β form a clearer pattern than those for He II.

Finally, we investigate the dependence of the broad line widths on the offsets between the line components. The results are shown in Fig. 11. We find that there is a clear correlation between the two parameters for H β , whereas there is again no single pattern in the He II data. If the offset is inversely correlated with the distance from the line-forming region to the SMBH, the behaviour of H β would be a typical presentation of AGN breathing. He II remarkably shows a trend in the opposite direction. This could indicate that the motion of the BLR where He II is formed is not purely set by Keplerian

kinematics. We return to the discussion and interpretation of this behaviour in Section 12.

7.2 Origin of scatter

The data in Figs 9, 10, and 11 show considerable scatter. The data for H β appear to show a clearer pattern than those for He II. A potential cause for the scatter that is intrinsic to MKN 110 is the relative quality of the fits: the He II line is considerably weaker than H β in all spectra, making the fit more sensitive to noise. This interpretation agrees with the fact that the scatter in Fig. 9 appears largest for the spectra at earlier epochs, when the He II line was relatively weak.

However, the scatter does not appear to be random: whereas the stacked result, which is made up almost exclusively of FAST-RM1 data, is consistent with the trend of the FAST-RM2 data, the later high-state data seem to be on a separate ‘branch’. This separation is much more significant for He II than for H β . If the scatter in the He II data is intrinsic to the AGN, this could imply that the response to a changing continuum is more erratic for gas closer to the central engine (such as for the gas that forms He II compared to the gas forming H β), or that the response of this gas can change on shorter time-scales. We return to this point in Section 10.

8 SUMMARY OF KEY RESULTS

8.1 Broad-line flux response effects

RI.1: Large variability. MKN 110 shows strong variability on time-scales of months to decades, in both the continuum (a factor of ~ 10) and the lines (up to a factor ~ 40 for He II 4686).

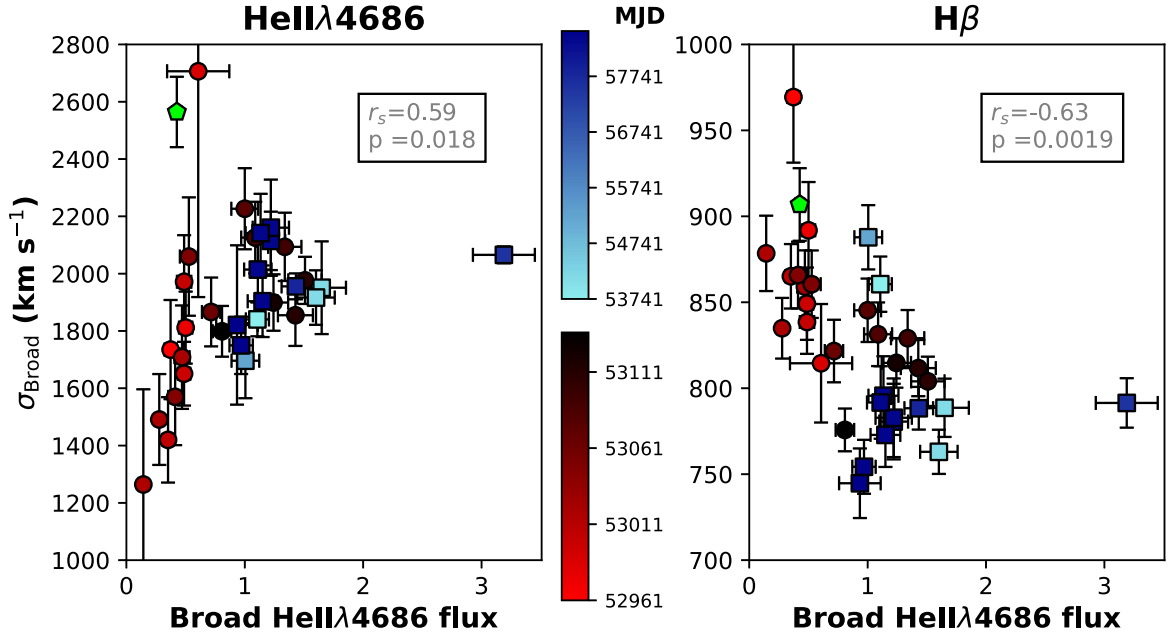


Figure 10. The width of the broad emission-line components plotted against the broad He II $\lambda 4686$ flux. The colours, shading, and correlation metrics are the same as in Fig. 9. For $H\beta$ we can see that the broad-line width decreases with increasing He II flux, an inverse correlation known as AGN breathing: as the luminosity (and the FUV flux) increases, the radius of the BLR increases, corresponding to a smaller rotational velocity and σ_{broad} of the BLR clouds. Interestingly, He II shows an opposite trend, which could indicate that the kinematics of the He II line-forming region are not purely Keplerian.

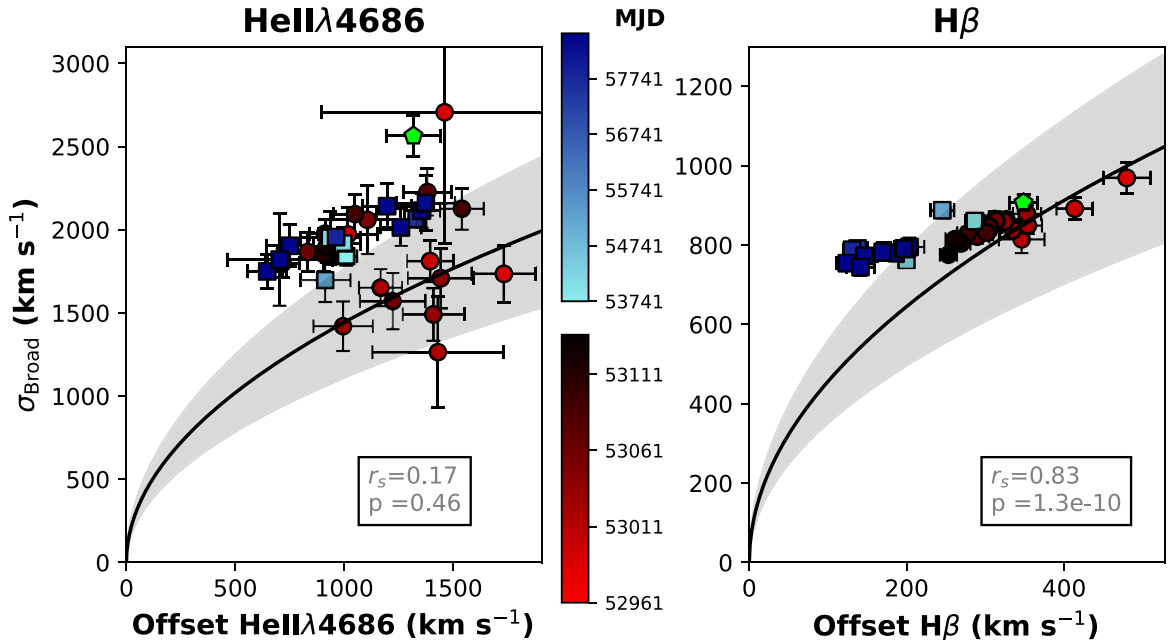


Figure 11. The line width of the broad component of He II $\lambda 4686$ (left-hand panel) and $H\beta$ (right-hand panel), plotted against the broad-to-narrow-line offsets. The colours, shading, and correlation metrics are as described for Fig. 9. There is a strong correlation between the parameters for $H\beta$, whereas the pattern for He II is considerably noisier. The black lines indicate the theoretical relation between offset and σ , if the offset is caused by gravitational redshift, for the case of a 21° inclination and virial factor $f = 4.1$. The shaded regions correspond to $\pm 5^\circ$ uncertainty, following the estimate from K03b.

R1.2: Extreme He II variability. Among the emission lines in the optical range, the variability is most pronounced for the high-ionization line He II $\lambda 4686$. This is in agreement with previous AGN variability studies, which show that the amplitude of variability correlates with the ionization level (Peterson 2008; Bentz et al. 2010).

The He II variability is *considerably stronger*, around a factor of 4, than that of the optical continuum, suggesting it is a proxy for the inaccessible FUV continuum variability.

R1.3: Differentiation in the emission line response. As the He II flux heads towards zero, other lines do not, with shifts of the order of

20–40 per cent of the normalized line flux. We correct for this non-responsive component by subtracting the fitted He II $\lambda 4686$ narrow-line flux (Section 5.2) and an offset for H α , H β , and He I $\lambda 5876$ (Section 6.2).

R1.4: Curvature in the emission line response. The response of the H α , H β , and He I $\lambda 5876$ emission lines to changes in the FUV flux (as indicated by He II $\lambda 4686$) is dependent on the level of incident flux. The line-emitting gas is less responsive at high FUV flux levels (Fig. 6). The effect can be approximated by a two-component function that has a flat response once it reaches a saturation level (Fig. 6). It is important to note that the full data set covers ~ 30 yr of observations. This means that the responsivity discussed here is different from the instantaneous responsivity previously investigated in photoionization models (e.g. O’Brien, Goad & Gondhalekar 1995; Korista & Goad 2004).

R1.5: Saturation-distance correlation. The level at which the response of the emission lines saturates, shows a negative correlation with the lags found in RM measurements (Fig. 7). This suggests that the saturation level for the lines is related to the physical location in the BLR or that it depends on the minimum ionization energy required to generate the line.

R1.6: Historical changes. The response of the lines to changes in the FUV differs from epoch to epoch. Over a time-scale of less than 5 yr, the response curve of a line is repeatable (i.e. going up and down in FUV flux has the same results), whereas data separated by 5–10 yr show a different line response (Fig. 8 and Table 6). A notable aspect of this slow-moving evolution is that some of response curves in Fig. 8 do not return to zero, even after our earlier removal of an average offset. This means that the fluxes from both the responsive and non-responsive material change with historical epoch.

8.2 Kinematic effects

R2.1: Velocity widths and velocity offsets change. As noted by K03b, the line profiles of He II $\lambda 4686$ and H β show a clear offset between the broad and narrow components. K03b, using a data set covering ~ 7 months, found that the offset is smaller for lines which have longer reverberation lags. In this study, where we make use of spectra taken over a period of ~ 16 yr, we find that the magnitude of both the offsets and the line widths evolve over time (Figs 9 and 10).

R2.2: Velocity offset versus flux. The broad-to-narrow-line velocity offset shows a negative correlation with the broad He II flux for the H β line (Fig. 9). This means that the velocity offsets are smaller at high flux states. The correlation is visible for H β , whereas the response of He II is more complex and possibly double-branched.

R2.3 Line width versus flux. The line width shows a negative correlation with the He II flux for H β (Fig. 10). He II, in contrast, shows overall a positive correlation, and again the behaviour is more complex.

R2.4: Line width versus offset. The line width of the broad component shows a strong and clear positive correlation with the offset for H β (Fig. 11). For He II we find no significant correlation.

R2.5: Contrast between He II and H β . As the ionizing flux varies, the H β line shows quite simple and consistent changes in velocity offset and line width. He II on the other hand shows no such clear trends. Although this can reflect uncertainties in the fitting process, this clear distinction likely indicates the large differences in kinematics between the two line-forming regions.

9 DISCUSSION: GENERAL POINTS

In the following discussion sections, we concentrate on model-independent implications, with some comments on specific models.

9.1 Black hole mass and scale alternatives

Interpretations depend on the observed lags and deduced masses, so we first summarize these. Based on the lags observed by K01, the BLR is clearly stratified, with the material dominating the He II, H β , and H α emission located at distances of $3.9^{+2.8}_{-0.7}$, $24.2^{+3.7}_{-3.3}$, and $32.3^{+4.3}_{-4.9}$ light-days respectively. However, the physical implications of these lags also depend on the assumed black hole mass. As discussed in Section 2, K02 and K03b represent the two extreme ends of the distribution of mass estimates. Based on the lags and the assumption that the line widths are set purely by Keplerian motion, KB02 derived $M_1 = 1.8 \times 10^7 M_\odot$. The above lags then correspond to $R/R_S = 1, 900, 11, 800,$ and $15\,700$ for He II, H β , and H α . Here R_S is the Schwarzschild radius. On the other hand, based on the assumption that line velocity offsets are caused by gravitational redshift, K03b derived $M_2 = 1.4 \times 10^8 M_\odot$. The line-lags then correspond to $R/R_S = 244, 1, 516,$ and 2023 . To make this second mass value consistent with the observed lags, K03b discusses a disc-wind model, in which we are seeing the MKN 110 system almost pole-on, at an inclination of 21° . In this case, there could well be a significant additional geometric correction factor in deducing the distance of the BLR clouds from the observed time lags. This large correction factor would mean the black hole mass deduced from the lags would also be significantly larger, reducing the tension between the gravitational-redshift mass estimate and the lag-based mass estimate.

9.2 Is MKN 110 representative?

There are two ways in which MKN 110 may be considered unusual for a broad-line type 1 AGN – the first is its large amplitude of variability and the second is the narrowness of the broad lines. Regarding the variability, there are other well-known historic examples of large changes in individual sources, for example NGC 1566 (Alloin et al. 1985), NGC 3516 (Ilić et al. 2020), Cen A (Lawrence, Pye & Elvis 1977), and NGC 4151 (Penston & Perez 1984). Recently, it has become clear that even high-luminosity quasars can show extreme variability over decadal time-scales. In a sample of approximately 100 000 quasars, MacLeod et al. (2016) found that ~ 1 per cent show magnitude changes $|\Delta g| > 1$ on time-scales smaller than 15 yr. Similarly, an estimated fraction of 30–50 per cent of quasars shows variability of $|\Delta g| > 1$ on time-scales greater than 15 yr (Rumbaugh et al. 2018), suggesting large changes in AGN are perhaps quite common.

Regarding line width, the Balmer lines are certainly narrower than for most type 1 AGN, and towards the upper end of what would traditionally be classed as NLSy1 (Osterbrock & Pogge 1985; Komossa 2008), although the He II width is more typical of AGN BLRs. For MKN 110 $\text{FWHM}_{H\beta} \sim 1940 \text{ km s}^{-1}$, on average; for NLSy1 typically $\text{FWHM}_{H\beta} < 2000 \text{ km s}^{-1}$ (Osterbrock & Pogge 1985), whereas ‘regular’ type 1 Seyferts have broad-line widths of thousands to tens of thousands km s^{-1} (Peterson 2006). Traditionally, there have been two rival explanations of the NLSy1 phenomenon: normal AGN seen close to pole-on, or objects with a high Eddington ratio, such that lines are formed further out. The current consensus is that the high-Eddington explanation is broadly correct, with perhaps a minority of objects being pole-on cases (Komossa 2008). MKN 110 could fit into either explanation. If the larger mass M_2 is correct, then

we are seeing MKN 110 at an inclination angle of 21° . An inclination this small or smaller will occur in ~ 6 percent of all AGNs, for random orientations. Alternatively, if the smaller mass M_1 is correct, then MKN 110 is marginally super-Eddington – $L/L_E \sim 1.4$ using the optical luminosity estimated by Bischoff & Kollatschny (1999) and a standard bolometric correction (Richards et al. 2006). As noted in Section 2, MKN 110 has very weak Fe II emission, and a normal X-ray spectrum and X-ray loudness, whereas most NLSy1s have strong Fe II, steep X-ray spectra, and are X-ray quiet (e.g. Lawrence et al. 1997). This may suggest that the ‘pole-on’ explanation is more likely; however, it is not conclusive.

In either of the above scenarios, MKN 110 is indeed unusual, but it remains a useful laboratory, to test ideas about the structure and physical nature of the BLR.

10 DISCUSSION: RESPONSE TIME-SCALES IN THE BLR

We observe non-linear line response repeatable over short time-scales, but not over longer ones (results R1.4, R1.5, R1.6). To understand this, it is useful to separate three kinds of BLR response – *reverberation*, *breathing*, and longer term *structural response*.

10.1 Reverberation

At the high densities, we understand to be present in BLR clouds, the recombination time-scale is of the order of hours, so, locally, clouds track changes in the ionizing continuum with negligible delay. We see those changes with a lag of the order of tens of days due to the finite size of the overall BLR system. The light curve of each line is a convolution of the continuum light curve, encoding the geometry and radial structure of the BLR. Using reverberation to deduce that structure is the focus of considerable effort in AGN monitoring.

10.2 Breathing of the BLR

For some AGN, it has been demonstrated that the observed lag changes from one reverberation campaign to another, and that the observed lag correlates with the mean luminosity during the campaign (Peterson et al. 1998; Peterson et al. 2002). The change in lag does not imply physical bulk motion; rather, this phenomenon is consistent with the basic insight of the ‘Locally Optimized Cloud’ (LOC) picture of Baldwin et al. (1995), that the BLR contains material with a wide range of distances, densities, and thicknesses, with the observed emission representing a weighted mean response over all this material. Because the response is sensitive to the ionization parameter, the radial location of that mean changes with luminosity. This phenomenon, of epoch-by-epoch shifting of the BLR response, has been referred to as ‘breathing’ (Korista & Goad 2004; Cackett & Horne 2006). The term ‘breathing’ is somewhat misleading as it implies a bulk motion, rather than the actual interpretation of ‘lighting up’ different regions within a fixed structure.

10.3 Structural response

In the breathing phenomenon, a fixed BLR structure responds passively to the changing luminosity. We then expect that the line-flux response to changing luminosity should be repeatable from one season to another. This is indeed what we see on \sim year time-scales, but on \sim decade time-scales, the response pattern changes. This suggests that on long enough time-scales, the BLR clouds themselves, and their distribution in space, physically respond to the

radiation from the central engine. This raises the question whether this is consistent with physical expectations.

For a variety of models, restructuring may occur on roughly the *dynamical time-scale* $t_d = \sqrt{R^3/GM}$ – for example if BLR clouds are condensations formed in a disc wind driven by the central radiation (Murray et al. 1995; Elvis 2000; Proga, Stone & Kallman 2000; Waters et al. 2016; Matthews et al. 2020). In this case t_d represents the time that material takes to travel through the BLR. At the $H\beta$ -lag radius of 24.2 light days, for the smaller black hole mass case M_1 we get $t_d = 10.2$ yr, and for the larger mass M_2 we get $t_d = 3.6$ yr. Therefore it is not sufficient to simply observe over several years. What is required is to observe changes in the luminosity smoothed over several years. From Fig. 2, it is clear that the long-term average has indeed changed from epochs I to II to III. We can then plausibly make the argument that we have detected the BLR dynamical time-scale in MKN 110.

Another possible cause for the observed long-term evolution is that individual BLR clouds are compressed by the central engine radiation, and so adjust their density structure, such as in the model presented by Baskin, Laor & Stern (2014) and Baskin & Laor (2018). This should occur on the *acoustic crossing time-scale* for a BLR cloud. For a cloud of thickness N_H , number density n_e , and temperature T we get

$$t_a = 2.7 \text{yr} \frac{N_H}{10^{23} \text{cm}^{-2}} \frac{10^9 \text{cm}^{-3}}{n_e}.$$

We therefore find that this is also a potential explanation of changes in the long-term response pattern. The clouds in the Baskin et al. (2014) model will maintain $U \sim 1$, as is expected for BLR material, even after significant changes in internal pressure.

A further clue comes from the kinematic changes seen in MKN 110’s broad emission lines. Correlations are seen among line width, offset, and flux (results R2.2, R2.3, R2.4), but while the changes in $H\beta$ are simple and consistent, He II shows a more complex behaviour (R2.5). This may be due to the shorter structural response time-scale of the He II emitting gas, causing hysteresis effects. For mass M_1 , while the dynamical time-scale at the $H\beta$ lag radius is 10.2 yr, for the He II lag radius of 3.9 light days we find a dynamical time-scale of 240 d, comparable to an observing season, so that the structure of the He II line-emitting regions may be substantially different from one year to the next, and even change significantly during a single season.

Like the dynamical time-scale, the acoustic time-scale may also be shorter for clouds closer in to the ionizing source (such as He II forming clouds compared to $H\beta$ forming clouds). This would be the case if the typical density of BLR clouds increases towards the centre of the system. However, whether this effect occurs is less clear than the difference in kinematic time-scales. Overall, the kinematic effects that we see thus add weight to the suggestion that in addition to the normal breathing, we are seeing the BLR physically respond on a mechanical time-scale, i.e. corresponding to gross motions or pressure waves.

11 DISCUSSION: THE SHAPE OF FLUX RESPONSE PATTERNS IN THE BLR

Grouping all epochs together, it seems that the BELs in MKN 110 have a curved response to changes in ionizing luminosity, in that the emission lines are less responsive at high luminosity (result R1.4). However, even with our large and long time-scale data set, it is still difficult to reliably distinguish instantaneous flux changes from historical changes (result R1.6). Nevertheless it seems clear

that responsivity is slower than proportional, and varies between line species, even for recombination lines. Furthermore, the relation between line flux and ionizing flux has a non-zero intercept, i.e. it seems that some of the BLR material does not respond to ionizing flux changes at all, even at low luminosity. We note that Fig. 6 shows responses after correcting for the non-responsive component average over all epochs, and Fig. 8 shows an epoch-dependent offset with respect to that global average offset.

11.1 Single cloud response

For the simplest single cloud models, thick clouds will be ionization bounded, with an ionized zone on the side facing the continuum source. The emitted flux for Hydrogen and Helium recombination lines should then be roughly proportional to continuum luminosity as the ionized zone increases in depth with higher luminosities. For heavier elements, and collisional lines, things are more complicated. Even for Hydrogen, for high density clouds, and with an SED extending into the X-rays, there are effects that have plagued AGN modellers for years, such as ionization from above the ground level, level-dependent line-transfer effects, and the effect of a partially ionized zone caused by X-rays (see e.g. Netzer 2013). None the less, line-luminosity should continue to increase with luminosity.

Thinner clouds could be matter bounded, i.e. fully ionized, so that a change in luminosity may produce no change in line flux at all. To produce a curved response including saturation, a cloud of intermediate thickness could be ionization bounded at low luminosity, and matter bounded at high luminosity, i.e. at high enough luminosity the ionizing radiation can penetrate the far side of the cloud. This transition mechanism was also proposed by Wamsteker & Colina (1986) to explain the diminishing response of the C IV λ 1550 line to continuum increases. As pointed out by Gaskell (2009), rather than a single thick cloud, there could be a series of overlapping, and so self-shielding, thinner clouds at different distances. As the luminosity increases, the clouds become fully ionized in radial sequence, inner clouds first.

11.2 Distributed cloud systems

As recognized in the LOC picture, the BLR is much more likely to be a system of clouds, with a wide distribution of densities, cloud thicknesses, radial distances, and covering factors. To calculate the net output requires photoionization calculations over a grid of cloud properties. In a series of papers, Goad, Korista, and collaborators have explored this idea thoroughly in the context of quite generic models with power-law distributions of those various quantities, e.g. Korista & Goad (2000), Korista & Goad (2004), Goad & Korista (2015). Such models clearly can produce curved responses, but the degrees of freedom in these generic models is rather large.

On the other hand, the geometry of the BLR in the context of the LOC model could play a significant role in explaining the striking nature of the patterns that we see in MKN 110. Ferland et al. (2020) observed a similar pattern for a single line (He II λ 4686) but using a sample of AGN spanning a sufficiently large range of luminosity. They attributed the emission-line deficit observed at the highest luminosities to a BLR with a toroidal geometry of a fixed scale height. If the fact that all three of our studied broad emission lines experience saturation at the highest He II line luminosities can be explained with such a toroidal geometry, their difference in saturation level could be explained if this BLR torus had a limit in radial extent. Such a limit to the BLR could be naturally provided by the onset of the dusty torus (Netzer & Laor 1993; Landt et al. 2014). However, this mechanism

only works if its inner radius was luminosity-invariant (Pott et al. 2010; Landt et al. 2019).

11.3 Non-responsive material

A distributed cloud system can produce a non-linear response, but the observation of differences in response (result R1.3) is most simply explained by the presence of material that does not respond to changes in the ionizing flux. One way to achieve this would be to consider multiple thin overlapping clouds, such as in the Gaskell (2009) picture. In this picture, the non-responsive material is nearer the middle. K03b compares mean and rms velocity profiles, and finds that for H α and H β the profiles are very similar in shape, suggesting that to first order the non-responsive material is distributed very similarly to the responsive material. The mean H α profile in the K03b data (judged by eye) may be somewhat broader than the rms profile, suggesting that there is more non-responsive material nearer the SMBH, contributing to non-variable emission in the line wings. In MKN 509, spectropolarimetry showed the line wings of H α are more polarized than the line centre, potentially indicating they are dominated by scattered light and therefore have a different behaviour than the line centre (Young et al. 1999; Lira et al. 2021). However, for both He I and He II, the rms profiles in MRK 110 are clearly broader than the mean profiles, suggesting that the non-responsive He II material is further out (contributing emission closer to centre of the line).

In a series of papers Devereux and collaborators have argued that some local AGN do not reverberate at all (e.g. Devereux 2018, and references therein), and that therefore BLR emission does not come from clouds, but from a large, optically thin, fully ionized region. Clearly in the MKN 110 case there is reverberating material, but it is possible that we have line flux contributions from both dense clouds and a thin medium in which the clouds are embedded. Rather than being a spherical Strömgren-sphere-like arrangement, this idea could fit well into disc-wind models. To go beyond this would need a specific model.

Finally we note that as the response slope changes over historical time (result R1.6), the offset also changes. The non-responsive material therefore also likely has a structural physical response to changes in luminosity, averaged over many years. There is both responsive and non-responsive material, and the amount of both gradually changes. This is an interesting parallel to the conclusion by Vincentelli et al. (2022), that the BLR contribution to the *continuum*, probably associated with an optically thin component, itself varies over time (on a time-scale of months), as a function of the continuum luminosity. Again we see that the BLR evolves on multiple time-scales, with structural changes occurring in MKN 110 on time-scales from years to decades.

12 DISCUSSION: KINEMATIC RESPONSE IN THE BLR

Here we look at the implications of results R2.2, R2.3, and R2.4. As noted in Section 10, the complexity of He II behaviour (result R2.5) is likely because of the short physical time-scales relevant to the He II emitting region, such that its structure is changing almost as fast as the continuum. This makes it very hard to interpret, and so for the rest of this section we concentrate on the behaviour of H β . The complexity of the behaviour of He II will add noise to the correlations among the He II flux and the parameters for H β .

Result R2.3, that velocity width decreases as ionizing flux increases, is qualitatively consistent with the idea that velocities are in

general gravity dominated and so roughly virial, together with the idea that as luminosity increases, clouds further out are lit up. It is hard to go beyond this to a quantitative prediction, as it is likely that the H β material covers a wide range of radii, and so a large range of velocities, at any one time.

To explain result R2.2, that velocity offset decreases as flux increases, we need to make an assumption as to what causes that offset. Below, we test several generic possibilities: (1) the offset is caused by a gravitational redshift of the broad line component; (2) the offset is caused by radial *infall* of the BLR material; (3) the offset is caused by a radial *outflow* of BLR material.

12.1 Gravitational redshift

If the velocity offset between the narrow and broad lines is caused by gravitational redshift, we can derive the expected relation between redshift and the line velocity width, the latter of which is still set by Keplerian motion. Expressed in terms of the gravitational radius R_g , the velocity offset due to gravitational redshift is given by $\Delta v_{gz} = c/\sqrt{R/R_g}$, where R is the radial distance from the SMBH. We can express the virial velocity in the same terms:

$$\sigma_v = \frac{c \sin(i)}{f \sqrt{R/R_g}} = \frac{\sqrt{c \Delta v_{gz} \sin(i)}}{f},$$

where i is the inclination, and f is the virial factor relating observed velocity width to virial velocity (Section 2). Fig. 11 shows this prediction for σ_{broad} as a function of the offset (Δv_{gz} in the expression above). For an inclination of $i = 21^\circ$ (Kollatschny 2003b) and a virial factor $f = 4.3$ (Grier et al. 2013), the model does not reproduce the shape of the correlation. For simplicity we show the relation for a specific value of f , rather than for a range of possible values; however, no value of f results in the right shape to match the data. We are implicitly assuming a single specific radius for the material, but the quadratic relationship should be the same at every radius, so it is not obvious that a distributed system of clouds can produce the right shape. A large mass with a pole on view produces a qualitative explanation for the discrepancy between the lag-based mass estimate and the estimate based on a presumed gravitational redshift; however, it does not fit the shape of the correlation that we find between line width and offset.

12.2 Infall

If the motion of the clouds has a net infall component, the near-side clouds appear redshifted, and the far-side clouds are blueshifted. Here we define ‘near-side clouds’ as the clouds that are on the same side of the SMBH as the observer, along the line of sight, and ‘far-side clouds’ as the clouds on the other side. In the case of infall, the near-side clouds are therefore moving away from us. To see a net redshift requires that the emission from the far-side clouds is systematically suppressed from along our line of sight. To investigate the possible configurations, we consider two cases: clouds that are optically thick in the H β transition and clouds that are optically thin in H β . In the optically thick case, the clouds will emit anisotropically, such that the side facing the nucleus is brighter. For almost all geometries this would result in the opposite effect – far-side clouds will appear brighter, as we are observing the parts of the far-side clouds facing the nucleus.

On the other hand, if the clouds are optically thin, we see them all equally well. Suppressing the far-side clouds could perhaps be achieved by blocking them from our view with the accretion disc

(such as found for Arp 151; Pancoast et al. 2014, 2018), provided it extends to large enough radii. The correlation between velocity width and offset then implies that the infall velocity is increasing inwards to the SMBH. This is generally consistent with any gravitational model. To go further requires a model that explains the relationship between rotation and infall.

In summary, for an infall model, clouds need to be optically thin, accelerating inwards, and with the far-side shielded by the disc.

12.3 Outflow

For a BLR in outflow, the emission from the far-side clouds is redshifted and the emission from the near-side ones blueshifted. As for the case of infall, if the clouds are optically thin, we see them all equally well. An occulting disc would result in the opposite effect – a net blueshift, as we only see the near-sided clouds. For optically thick, anisotropic clouds, we preferentially see the far-side ones (the parts facing the nucleus), so this picture naturally gives a net redshift as long as there is *not* an occulting disc. The width-offset correlation then implies that the clouds are decelerating as they move radially outward.

Outward deceleration is not what would be predicted for a radiation-pressure driven outflow. However, this behaviour could result from a ballistic outflow, which receives an initial impulse nearer the central source and then decelerates under gravity. However, the deceleration would be very fast – the offset velocity changes by a factor of five, while the velocity width changes by about 25 per cent. This implies the presence of a drag force, as proposed in the ‘Quasar Rain’ model of Elvis (2017). In this model, a thin disc wind is radiatively accelerated at some radius on the disc, and the BEL clouds are condensations which form within this wind. The clouds have a very different (lower) radiative force multiplier than the surrounding wind, so they stop accelerating, and furthermore suffer a drag force from the wind. In the end, the clouds fall back towards the disc. In this scenario, we could expect to observe both outflow and infall, associated with different clouds.

12.4 Rotation with projection effects

Finally, we note that apparent velocity offsets can be achieved without a radial velocity component, by projection effects. Consider, for example the case where the BELs are condensations in a conical structure which is primarily rotating, even if it also has an outflow component (e.g. Elvis 2000). If the clouds are optically thick and therefore emitting anisotropically, the line radiation will effectively arise from the inner surface wall of the cone, with the rotational Doppler shift varying with position around the cone wall. However, the $\cos \theta$ projection effect (θ with respect to our line of sight) will also vary with position around the wall, which can result in a velocity-dependent suppression. The degree of observed shift will depend on both the opening angle of the cone and the tilt angle towards the viewer - it is possible to result in either net redshifts or net blueshifts. The observation that the amount of offset depends on the velocity width suggests that the cone opening angle increases with larger radii, such as proposed in the model of Elvis (2017). We leave a detailed comparison of this model to future work.

13 CONCLUSIONS

The strongly variable output and extensive history of optical monitoring campaigns make MKN 110 an excellent test case for our study of the long-term evolution of the BLR response. Our data set covers

30 yr of spectroscopic observations and provides a uniquely detailed view of the evolution of the BLR on this long time-scale. We find that using He II $\lambda 4686$ as a proxy of the FUV continuum provides a promising method to understand and interpret the behaviour of the lower ionization lines. We observe a levelling off of the responsivity of the ionization lines at higher He II $\lambda 4686$ levels. In our two-component model we fit this behaviour as a saturation level of the response. The stratification of the saturation levels in the line response corresponds with the physical stratification of the line species, as evident from RM studies. This suggests we are seeing the effect of key physical processes in the regulation of BLR emission.

In studying the profiles of the He II $\lambda 4686$ and H β lines, we find that the change in velocity offset between the narrow and broad line components does not fully match expectations, if we assume that the offset is caused by a gravitational redshift of the broad-line component. We explore several alternative explanations for the observed evolution, in which the offset is caused by bulk motion of the broad-line emitting gas. We find several generic models that explain the observed behaviour. However, the response of the BLR to a changing continuum is complex, as perhaps best exemplified by the difference in behaviour between He II $\lambda 4686$ and H β . This complexity emphasizes the need for a more sophisticated, physical BLR model. Such a model lies outwith the scope of this publication.

The detailed behaviour that we are able to observe, emphasizes the analytical power provided by long-term observations, and in particular by repeated spectroscopy, in the study of AGN. The data set available for MKN 110 is currently rare, both in its duration and its detail. However, we can look forward to the results from new spectroscopic surveys, such as SDSS-V, that will increase the number of objects where we can study the evolution of the BLR using the techniques outlined in this paper.

ACKNOWLEDGEMENTS

DH acknowledges support from the Deutsches Zentrum fuer Luft- und Raumfahrt (DLR) grant FKZ 50 OR 2003, as well as from a previous Principal's Career Development PhD Scholarship from the University of Edinburgh. HL acknowledges a Daphne Jackson Fellowship sponsored by the Science and Technology Facilities Council (STFC), UK. This study has made extensive use of the fluxes published in BK99 and K01 and the authors wish to express their gratitude for the inclusion of these data-sets in their entirety in the aforementioned works. For the FAST spectra, this paper uses data products produced by the OIR Telescope Data Center, supported by the Smithsonian Astrophysical Observatory.

DATA AVAILABILITY

All fluxes, spectra, spectral fitting results, and the code needed to create the figures presented in this work are available at <https://github.com/dshoman/MKN110>.

REFERENCES

Afanasiev V. L., Popović L. Č., Shapovalova A. I., 2019, *MNRAS*, 482, 4985
 Alloin D., Pelat D., Phillips M., Whittle M., 1985, *ApJ*, 288, 205
 Baldwin J., Ferland G., Korista K., Verner D., 1995, *ApJ*, 455, L119
 Barth A. J. et al., 2015, *ApJS*, 217, 26
 Baskin A., Laor A., 2018, *MNRAS*, 474, 1970
 Baskin A., Laor A., Stern J., 2013, *MNRAS*, 438, 604
 Baskin A., Laor A., Stern J., 2014, *MNRAS*, 445, 3025
 Bentz M. C. et al., 2010, *ApJ*, 716, 993

Bentz M. C. et al., 2013, *ApJ*, 767, 149
 Bischoff K., Kollatschny W., 1999, *A&A*, 345, 49
 Blandford R. D., McKee C. F., 1982, *ApJ*, 255, 419
 Boller T., Balestra I., Kollatschny W., 2007, *A&A*, 465, 87
 Cackett E. M., Horne K., 2006, *MNRAS*, 365, 1180
 Cackett E. M., Gültekin K., Bentz M. C., Fausnaugh M. M., Peterson B. M., Troyer J., Vestergaard M., 2015, *ApJ*, 810, 86
 Clavel J. et al., 1991, *ApJ*, 366, 64
 Condon J. J., 1992, *ARA&A*, 30, 575
 Dalla Bontà E. et al., 2020, *ApJ*, 903, 112
 Devereux N., 2018, *MNRAS*, 473, 2930
 Done C., Davis S. W., Jin C., Blaes O., Ward M., 2012, *MNRAS*, 420, 1848
 Eastman R. G., MacAlpine G. M., 1985, *ApJ*, 299, 785
 Elvis M., 2000, *ApJ*, 545, 63
 Elvis M., 2017, *ApJ*, 847, 56
 Fabricant D., Cheimets P., Caldwell N., Geary J., 1998, *PASP*, 110, 79
 Fausnaugh M. M. et al., 2016, *ApJ*, 821, 56
 Ferland G. J., Done C., Jin C., Landt H., Ward M. J., 2020, *MNRAS*, 494, 5917
 Ferrarese L., Merritt D., 2000, *ApJ*, 539, L9
 Ferrarese L., Pogge R. W., Peterson B. M., Merritt D., Wandel A., Joseph C. L., 2001, *ApJ*, 555, L79
 Fitzpatrick E. L., 1999, *PASP*, 111, 63
 Gaskell C. M., 2009, *New Astron. Rev.*, 53, 140
 Gaskell C. M., Sparke L. S., 1986, *ApJ*, 305, 175
 Gliozzi M., Titarchuk L., Satyapal S., Price D., Jang I., 2011, *ApJ*, 735, 16
 Goad M. R. et al., 2019, *MNRAS*, 486, 5362
 Goad M. R., Korista K. T., 2015, *MNRAS*, 453, 3662
 Goad M. R., O'Brien P. T., Gondhalekar P. M., 1993, *MNRAS*, 263, 149
 Greene J. E., Ho L. C., 2006, *ApJ*, 641, L21
 Grier C. J. et al., 2012, *ApJ*, 744, L4
 Grier C. J. et al., 2013, *ApJ*, 764, 47
 Grupe D., 2004, *AJ*, 127, 1799
 Grupe D., Thomas H. C., Beuermann K., 2001, *A&A*, 367, 470
 Gunn J. E. et al., 2006, *AJ*, 131, 2332
 Guo H., Sun M., Liu X., Wang T., Kong M., Wang S., Sheng Z., He Z., 2019, *ApJ*, 883, L44
 Homan D., MacLeod C. L., Lawrence A., Ross N. P., Bruce A., 2020, *MNRAS*, 496, 309
 Ilić D. et al., 2020, *A&A*, 638, A13
 Jin C., Ward M., Done C., 2012, *MNRAS*, 425, 907
 Kaspi S., Smith P. S., Netzer H., Maoz D., Jannuzi B. T., Giveon U., 2000, *ApJ*, 533, 631
 Kelly B. C., Bechtold J., Siemiginowska A., 2009, *ApJ*, 698, 895
 Kollatschny W., 2003a, *A&A*, 407, 461 (K03a)
 Kollatschny W., 2003b, *A&A*, 412, L61 (K03b)
 Kollatschny W., Bischoff K., 2002, *A&A*, 386, L19
 Kollatschny W., Bischoff K., Robinson E. L., Welsh W. F., Hill G. J., 2001, *A&A*, 379, 125
 Komossa S., 2008, *Rev. Mex. Astron. Astrofis. Ser. Conf.*, 32, 86
 Korista K., Ferland G., Baldwin J., 1997, *ApJ*, 487, 555
 Korista K. T., Goad M. R., 2000, *ApJ*, 536, 284
 Korista K. T., Goad M. R., 2004, *ApJ*, 606, 749
 Kozłowski S. et al., 2010, *ApJ*, 708, 927
 Krolik J. H., Horne K., Kallman T. R., Malkan M. A., Edelson R. A., Kriss G. A., 1991, *ApJ*, 371, 541
 Kubota A., Done C., 2018, *MNRAS*, 480, 1247
 LaMassa S. M. et al., 2015, *ApJ*, 800, 144
 Landt H. et al., 2019, *MNRAS*, 489, 1572
 Landt H., Bentz M. C., Ward M. J., Elvis M., Peterson B. M., Korista K. T., Karovska M., 2008, *ApJS*, 174, 282
 Landt H., Elvis M., Ward M. J., Bentz M. C., Korista K. T., Karovska M., 2011, *MNRAS*, 414, 218
 Landt H., Ward M. J., Elvis M., Karovska M., 2014, *MNRAS*, 439, 1051
 Lawrence A., Pye J. P., Elvis M., 1977, *MNRAS*, 181, 93P
 Lawrence A., Elvis M., Wilkes B. J., McHardy I., Brandt N., 1997, *MNRAS*, 285, 879
 Lira P. et al., 2018, *ApJ*, 865, 56

- Lira P. et al., 2021, *MNRAS*, 507, 579
- Liu H. T., Feng H. C., Bai J. M., 2017, *MNRAS*, 466, 3323
- MacLeod C., Ross N., Lawrence A., Goad M., Horne K., 2016, *MNRAS*, 457, 389
- Mathews W. G., Ferland G. J., 1987, *ApJ*, 323, 456
- Matthews J. H., Knigge C., Higginbottom N., Long K. S., Sim S. A., Mangham S. W., Parkinson E. J., Hewitt H. A., 2020, *MNRAS*, 492, 5540
- McLure R. J., Dunlop J. S., 2004, *MNRAS*, 352, 1390
- Meléndez M., Kraemer S. B., Weaver K. A., Mushotzky R. F., 2011, *ApJ*, 738, 6
- Meyer-Hofmeister E., Meyer F., 2011, *A&A*, 527, A127
- Murray N., Chiang J., Grossman S. A., Voit G. M., 1995, *ApJ*, 451, 498
- Netzer H., 2013, *The Physics and Evolution of Active Galactic Nuclei*. Cambridge Univ. Press, Cambridge. Available at: <https://ui.adsabs.harvard.edu/abs/2013peag.book.....N>
- Netzer H., 2020, *MNRAS*, 494, 1611
- Netzer H., 2022, *MNRAS*, 509, 2637
- Netzer H., Laor A., 1993, *ApJ*, 404, L51
- Nicastro F., 2000, *ApJ*, 530, L65
- O'Brien P. T., Goad M. R., Gondhalekar P. M., 1995, *MNRAS*, 275, 1125
- Osterbrock D. E., Ferland G. J., 2006, *Astrophysics of Gaseous Nebulae and Active Galactic Nuclei*. University Science Books, Sausalito, CA. Available at: <https://ui.adsabs.harvard.edu/abs/2006agna.book.....O>
- Osterbrock D. E., Pogge R. W., 1985, *ApJ*, 297, 166
- Paltani S., Courvoisier T. J. L., 1994, *A&A*, 291, 74
- Pancoast A. et al., 2018, *ApJ*, 856, 108
- Pancoast A., Brewer B. J., Treu T., Park D., Barth A. J., Bentz M. C., Woo J.-H., 2014, *MNRAS*, 445, 3073
- Panda S., Czerny B., Done C., Kubota A., 2019, *ApJ*, 875, 133
- Panessa F. et al., 2022, *MNRAS*, 510, 718
- Penston M. V., Perez E., 1984, *MNRAS*, 211, 33P
- Peterson B. M. et al., 1992, *ApJ*, 392, 470
- Peterson B. M. et al., 2000, *ApJ*, 542, 161
- Peterson B. M. et al., 2002, *ApJ*, 581, 197
- Peterson B. M. et al., 2004, *ApJ*, 613, 682
- Peterson B. M. et al., 2013, *ApJ*, 779, 109
- Peterson B. M. et al., 2014, *ApJ*, 795, 149
- Peterson B. M., 1988, *PASP*, 100, 18
- Peterson B. M., 1993, *PASP*, 105, 247
- Peterson B. M., 2006, in Alloin D., ed., *Physics of Active Galactic Nuclei at all Scales*, LNP Vol. 693. Springer, Berlin, 77. Available at: <https://ui.adsabs.harvard.edu/abs/2006LNP...693...77P>
- Peterson B. M., 2008, *New Astron. Rev.*, 52, 240
- Peterson B. M., Ferland G. J., 1986, *Nature*, 324, 345
- Peterson B. M., Wanders I., Bertram R., Hunley J. F., Pogge R. W., Wagner R. M., 1998, *ApJ*, 501, 82
- Ponti G., Papadakis I., Bianchi S., Guainazzi M., Matt G., Uttley P., Bonilla N. F., 2012, *A&A*, 542, A83
- Porquet D., Reeves J. N., Grosso N., Braito V., Lobban A., 2021, *A&A*, 654, A89
- Pott J.-U., Malkan M. A., Elitzur M., Ghez A. M., Herbst T. M., Schödel R., Woillez J., 2010, *ApJ*, 715, 736
- Proga D., Stone J. M., Kallman T. R., 2000, *ApJ*, 543, 686
- Rees M. J., Netzer H., Ferland G. J., 1989, *ApJ*, 347, 640
- Richards G. T. et al., 2006, *ApJS*, 166, 470
- Rumbaugh N. et al., 2018, *ApJ*, 854, 160
- Stoughton C. et al., 2002, *AJ*, 123, 485
- Sun M. et al., 2015, *ApJ*, 811
- Tokarz S. P., Roll J., 1997, in Hunt G., Payne H., eds, *ASP Conf. Ser. Vol. 125, Astronomical Data Analysis Software and Systems VI*. Astron. Soc. Pac., San Francisco, p. 140
- van Dokkum P. G., Bloom J., Tewes M., 2012, *L.A. Cosmic: Laplacian Cosmic Ray Identification*, Astrophysics Source Code Library, record (ascl:1207.005)
- Vaughan S., Edelson R., Warwick R. S., Uttley P., 2003, *MNRAS*, 345, 1271
- Véron-Cetty M. P., Joly M., Véron P., 2004, *A&A*, 417, 515
- Véron-Cetty M. P., Véron P., Joly M., Kollatschny W., 2007, *A&A*, 475, 487
- Vincentelli F. M. et al., 2021, *MNRAS*, 504, 4337
- Vincentelli F. M., McHardy I., Hernández Santisteban J. V., Cackett E. M., Gelbord J., Horne K., Miller J. A., Lobban A., 2022, *MNRAS*, 512, L33
- Wamsteker W., Colina L., 1986, *ApJ*, 311, 617
- Waters T., Kashi A., Proga D., Eracleous M., Barth A. J., Greene J., 2016, *ApJ*, 827, 53
- Webb W., Malkan M., 2000, *ApJ*, 540, 652
- Williams J. K., Gliozzi M., Rudzinsky R. V., 2018, *MNRAS*, 480, 96
- Winter L. M., Veilleux S., McKernan B., Kallman T. R., 2012, *ApJ*, 745, 107
- Young S., Corbett E. A., Giannuzzo M. E., Hough J. H., Robinson A., Bailey J. A., Axon D. J., 1999, *MNRAS*, 303, 227

SUPPORTING INFORMATION

Supplementary data are available at *MNRAS* online.

Table 3. Overview of the flux data used in this paper, combining the results from multiple data sets.

Table 4. The results of our spectral fitting of the He II $\lambda 4686$ and H β lines.

Please note: Oxford University Press is not responsible for the content or functionality of any supporting materials supplied by the authors. Any queries (other than missing material) should be directed to the corresponding author for the article.

This paper has been typeset from a $\text{\TeX}/\text{\LaTeX}$ file prepared by the author.